Evolution of coseismic and post-seismic landsliding after the 2015 M_w 7.8 Gorkha earthquake, Nepal

Mark E. Kincey[1], Nick J. Rosser[1], Tom R. Robinson[2], Alexander L. Densmore[1], Ram Shrestha[3], Dammar Singh Pujara[3], Katie J. Oven[4], Jack G. Williams[1,5] and Zuzanna M. Swirad[1,6]

[1] Institute of Hazard, Risk, and Resilience and Department of Geography, Durham University, Durham, UK

[2] School of Geography, Science, and Politics, Newcastle University, Newcastle-Upon-Tyne, UK

[3] National Society for Earthquake Technology-Nepal, Kathmandu, Nepal

[4] Department of Geography and Environmental Sciences, Northumbria University, Newcastle-Upon-Tyne, UK

[5] Willis Towers Watson, Friars Street, Ipswich, Suffolk, UK

[6] Scripps Institution of Oceanography, University of California San Diego, La Jolla, CA, USA

Corresponding author: Mark Kincey (m.e.kincey@durham.ac.uk)

Abstract

Coseismic landslides are a major hazard associated with large earthquakes in mountainous regions. Despite growing evidence for their widespread impacts and persistence, current understanding of the evolution of landsliding over time after large earthquakes, the hazard that these landslides pose, and their role in the mountain sediment cascade remains limited. To address this, we present the first systematic multi-temporal landslide inventory to span the full rupture area of a large continental earthquake across the pre-, co- and post-seismic periods. We focus on the 3.5 years since the 2015 M_w 7.8 Gorkha earthquake in Nepal and show that throughout this period both the number and area of mapped landslides have remained higher than on the day of the earthquake itself. We document systematic upslope and northward shifts in the density of landsliding through time. Areas where landslides have persisted tend to cluster in space, but those areas that have returned to pre-earthquake conditions are more dispersed. Whilst both pre- and coseismic landslide locations tend to experience persistent post-earthquake landsliding, a wider population of newly activated but spatially-dispersed landslides has developed after the earthquake. This is particularly important for post-earthquake recovery plans that are typically based on hazard assessments conducted immediately post-earthquake and thus do not consider the evolving landslide hazard. We show that recovery back to pre-earthquake landsliding rates is fundamentally dependent on how that recovery is defined and measured. Clarity around this definition is particularly important for informing a comprehensive and precautionary approach to post-earthquake landslide hazard and risk.

1. Introduction

Coseismic landslides represent a major cascading hazard associated with high-magnitude earthquakes in mountainous environments (Fan et al., 2019). The widespread landsliding observed in many recent large continental earthquakes has led to substantially higher death tolls (Budimir et al., 2014), disruption to infrastructure (Bird and Bommer, 2004; Aydin et al., 2018), and the mobilisation and transport of large volumes of sediment (Huang and Montgomery, 2012; Wang et al., 2015). Increased interest in understanding the spatial distribution, impacts, and timing of coseismic landslides in recent decades has resulted in the production of a growing number of coseismic landslide inventories (Tanyas et al., 2017). In contrast, despite growing evidence for the persistence of enhanced landslide rates and the consequent long-term impacts of coseismic hillslope damage in the years to decades after a major earthquake (e.g., Dadson et al., 2004; Hovius et al., 2011; Marc et al., 2015; Parker et al., 2015), our current understanding of the post-seismic evolution of landslides is limited. As a result, we remain incapable of anticipating the spatio-temporal evolution of landslide hazard after a large earthquake, which frustrates our ability to inform response, recovery, and reconstruction (e.g., Robinson et al., 2017; Williams et al., 2018), and limits understanding of the long-term role of earthquakes in the overall mountain sediment cascade.

A standard approach to tracking post-seismic landsliding is to develop multi-temporal landslide inventories, usually by mapping from airborne or satellite imagery. This is a time-consuming and potentially expensive process, however, with the result that much of our existing understanding of post-seismic landsliding comes from just two earthquakes: the 1999 M_w 7.6 Chi-Chi earthquake in Taiwan, and the 2008 M_w 7.9 Wenchuan earthquake in China. The Chi-Chi earthquake triggered >20,000 landslides and elevated suspended sediment concentrations in rivers draining the affected area by a factor of four relative to decadal background levels (Dadson et al., 2004). Analysis of stream gauge data and time series

landslide mapping following this event suggested a post-seismic decay in suspended sediment flux (Hovius et al., 2011) and the rate of new landsliding (Marc et al., 2015) that returned to pre-event levels within approximately six years. Marc et al. (2015) extended this analysis to three other shallow thrust-faulting earthquakes, demonstrating that the rate of new landslide occurrence peaked immediately after each event and then decayed to pre-event values within 1-4 years, with the recovery time tentatively suggested to be proportional to earthquake magnitude. Khan et al. (2013) and Barth et al. (2019) suggested similarly short recovery times after the 2005 M_w 7.6 Kashmir and 2012 M_w 7.8 Haida Gwaii earthquakes, respectively. This recovery time is a critical factor in post-seismic landslide hazard, because it determines the time period over which persistent and repeated disruption might be expected across the earthquake-affected area.

In contrast, studies of the Wenchuan earthquake have suggested a more complex response, with a wide range in inferred recovery times. The earthquake triggered >60,000 landslides over an area of >100,000 km^2 (Dai et al., 2011; Xu et al., 2014). A large and growing number of studies have assessed spatio-temporal changes in the occurrence of new landslides as well as the remobilisation and transport of pre- and coseismic landslide debris. These studies have used a variety of approaches, but have tended to focus on small portions of the overall landslide-affected area. For example, Fan et al. (2018; 2019) compiled four post-earthquake inventories over a 463 km^2 area near the epicentre (~0.4% of the total affected area). New post-seismic landslides made up less than 10% of each of their inventories; instead, post-earthquake landslide activity was dominated by remobilisation of existing landslide scars and their deposits into debris flows. Both the proportion of landslides that were remobilised and the extent of remobilisation declined over time, returning to background levels within approximately seven years. Similarly, Tang et al. (2016) compiled six inventories spanning 2005-2015 over a 172 km^2 area near the epicentre (~0.1% of the affected area), demonstrating a 100-fold decrease in the number of active landslides in the seven years after the earthquake. While most post-earthquake landsliding occurred in the first three years, landslide rates had still not decayed to pre-earthquake levels by the end of their study. In contrast, other studies have argued that the rates of landsliding (e.g., Huang and Li, 2014) or post-seismic debris flows (e.g., Zhang and Zhang, 2017) are likely to remain elevated for several decades, with Li et al. (2018) speculating that a full return to pre-earthquake conditions could take 50-100 years. Studies of vegetation damage and recovery, using satellite image-based vegetation proxies (e.g., Yang et al., 2018; Ni et al., 2019; Yunus et al., 2020; Shen et al., 2020; Chen et al., 2020), have also tended to infer longer recovery times, on the order of several decades, but have pointed to strong spatial heterogeneities in recovery, with time scales expected to be longer in the areas with the highest density of coseismic landslides (Ni et al., 2019).

These disparities in inferred recovery time likely stem from two separate sources: (1) real differences in recovery time between different earthquakes, which we would like to understand, and (2) differences in definition, methodology, and resolution, which we would like to correct for. Even the term ‘recovery’ is used in a range of ways, from a decline in the rate of new landslides or debris flows to pre-earthquake values, to stabilisation of coseismic landslide debris, to the re-establishment of pre-earthquake vegetation. There is little consensus on whether to focus solely on the occurrence of new post-earthquake landslides on previously-unfailed hillslopes or on the continued evolution of pre- and coseismic landslide scars. For example, landslide rates following the 2005 Kashmir earthquake differ markedly depending on the specific method used to generate the inventory, with full recovery estimates ranging from <5 years (Khan et al., 2013) to >13 years (Shafique, 2020). Inventories that

contain only new landslides can show a rapid post-earthquake decline in landslide rates (e.g., Marc et al., 2015), but will underpredict the hazard from pre-seismic or coseismic landslides that remain active. Identifying landslides that remain active but which have not changed overall shape or size in a distinct, measurable way is problematic without detailed field surveys, often resulting in only broad definitions of activity. There is evidence, however, that the hazard posed by landslides can persist, even when the overall mapped footprint does not change. For example, in their field-based study of landslide development along two critical highways in Nepal in the three years following the 2015 M_w 7.8 Gorkha earthquake, Tian et al. (2020) documented repeated activity and continued hazard across the majority of sites investigated. Importantly, this included landslides that had not changed in overall size but had either reactivated or had undergone a change in dominant failure mechanism, such as from dry debris cascades to wet debris flows. Increasing revegetation of a coseismic landslide was also not necessarily indicative of a cessation of hazard, with five revegetating landslides noted as still active three years after the earthquake. Multi-temporal inventories that focus solely on new or substantially-altered landslide footprints may potentially therefore underestimate the overall level of landslide hazard, and potentially overstimate the wider rate of landscape recovery.

In addition, many studies have focused on only small portions of the total earthquake-affected area, despite growing evidence of strong spatial variations in both post-seismic landsliding and recovery (e.g., Yunus et al., 2020; Shen et al., 2020). Differences in methodology may play a role as well; airborne and satellite images are well-suited for distinguishing between vegetated and unvegetated areas, but not for determining the stability of the ground surface or the extent of landslide activity and downslope transport (Bernard et al., In Review). Indirect measures of landslide activity, such as downstream suspended-sediment discharge (e.g., Dadson et al., 2004; Wang et al., 2015; Zhang et al., 2019), may reflect changes in sediment supply or transfer to rivers rather than changes in landslide activity. Comparison of such direct and indirect measures relies on a comprehensive understanding of sediment transport pathways and storage within the landscape which is often lacking. Finally, it is also important to recall that recovery of landslide rates to pre-earthquake levels is not synonymous with the removal of all coseismic landslide debris from the landscape. Careful documentation of debris volumes and transport in portions of the Wenchuan earthquake rupture area has demonstrated that >80% of the material liberated by coseismic landsliding continued to reside on hillslopes or in low-order channels after a decade (Huang and Li, 2014; Zhang and Zhang, 2017; Fan et al., 2018). This suggests that the response to large earthquakes evolves over multiple overprinting time scales: relatively short-term changes in the rate of new and persistent mass wasting on the one hand, and long-term enhancement of erosion rates and sediment flux due to hillslope damage and sustained high rates of sediment supply on the other (Fan et al., 2018).

Together, these issues mean that we do not yet have a comprehensive picture of how landslide inventories evolve in space and time after a large earthquake, despite the importance of this picture for understanding dynamic landslide hazard and the associated risk. To begin to address this gap, we document coseismic and post-seismic landsliding across the area that was significantly impacted by the 2015 M_w 7.8 Gorkha earthquake in Nepal over the period 2014-2018. We use a consistent mapping methodology, based on pre- and post-monsoon medium-resolution satellite imagery, that is designed to optimise our ability to assess change through time. Critically, we map each of the eleven time epochs independently and in full, resulting in an internally-coherent set of eleven inventories that each include all visible landslides at each point in time. As a result, our approach deliberately

accounts for the persistence and evolution of pre-existing landslides, rather than just the occurrence of new failures, providing an alternative perspective on the rate of post-seismic landscape recovery. This allows the first documentation of both the evolution of the total distribution of landslide activity and detailed shifts in landslide form and location resulting from the earthquake and the four subsequent monsoon seasons.

2. The 2015 M_w 7.8 Gorkha earthquake and landslide inventories

The 25 April 2015 M_w 7.8 Gorkha earthquake initiated ~80 km northwest of Kathmandu in the district of Gorkha, with rupture propagating eastwards for ~140 km along the Main Himalayan Thrust (MHT) (Avouac et al., 2015). A series of large aftershocks followed, including a M_w 7.3 event on 12 May ~75 km east-northeast of Kathmandu in Dolakha district (Fig. 1). Intense shaking triggered extensive landsliding across the east-west extent of fault rupture, with the density of landslides generally increasing towards the east (Martha et al., 2017). Multiple coseismic landslide inventories have been produced for the Gorkha event (e.g., Kargel et al., 2016; Martha et al., 2017; Xu et al., 2016; Tiwari et al., 2017; Roback et al., 2018; Williams et al., 2018; Meena and Piralilou, 2019), resulting in estimates of landslide numbers ranging from <5,000 to ~25,000. The most detailed assessment, and therefore probably the most complete inventory to date, was produced from high-resolution satellite imagery by Roback et al. (2018) and documented ~25,000 landslides with a combined area of ~90 km^2, distributed across an area of 28,300 km^2 of central Nepal.

Assessments of post-seismic landslide rates and distributions are so far fairly limited for the Gorkha earthquake sequence. Tian et al. (2020) used imagery and field surveys to document the evolution of c. 30 landslides along two major highway corridors. They found that most of the landslides enlarged or remained active through the first three years after the earthquake, with frequent remobilisation of pre- and co-seismic landslide material into debris flows. Marc et al. (2019) suggested that rainfall-induced landslide rates in three selected catchments covering 7% of the total affected area were ~3-6 times higher for the 2015 monsoon when compared to pre-earthquake levels. Between 70-80% of the landslides in their 2015 monsoon inventory were in new locations when compared with the coseismic landslides from Roback et al. (2018), suggesting that new failures occurred on hillslopes weakened by the earthquake rather than by reactivation of pre-existing landslides. By 2017, the rate of new rainfall-induced landslides in all three catchments had returned to pre-earthquake levels (Marc et al., 2019). Enhanced rates of post-seismic debris flows also appear to have been relatively short-lived, with the exhaustion of loose material mobilised from coseismic failures during the 2015 monsoon and a reduction in the number of new debris flows back to pre-earthquake levels by 2016 (Dahlquist and West, 2019). Dahlquist and West (2019) reported that only ~2% of coseismic landslides developed into post-seismic debris flows, with the majority of failures likely to either be in more stable hillslope positions (Dahlquist and West, 2019) or directly coupled with fluvial channels and so exhausted of loose sediment immediately following the earthquake (Roback et al., 2018).

3. Data and methodology

3.1 Landslide inventory mapping

We mapped landslides from a time series of freely-available medium-resolution satellite imagery (Landsat and Sentinel-2) covering the period from 2014 to 2018, and focusing on an

area of 25,575 km^2 covering the 14 administrative districts that were most intensively affected by the 2015 Gorkha earthquake, as identified by the Government of Nepal (Fig. 1) This represents just over 90% of the landslide-affected area mapped by Roback et al. (2018). Mapping was divided into eleven individual epochs, including pre- and post-monsoon inventories for each individual year, as well as an additional coseismic inventory for 2015 (Table 1). Landsat 8 imagery was used for epochs 1-5 (2014-2015), with the lower resolution (30 m) multispectral bands being pan-sharpened to 15 m resolution using the panchromatic band 8. Panchromatic sharpening involves the radiometric transformation of a lower spatial resolution multiband image using a higher resolution image band, effectively increasing the spatial resolution of the original colour image to provide enhanced detail. We then switched to Sentinel-2 imagery (10 m spatial resolution) when coverage became available from epoch 6 (pre-monsoon 2016) onwards. Medium-resolution imagery was chosen because it spans the full pre- and post-earthquake time period, allows for low-cost long-term monitoring over the entire earthquake-affected area, and suffers less geometric distortion compared to high resolution imagery, which is a particular problem in high-relief environments (Weiss and Walsh, 2009). For each epoch, we chose images that spanned the shortest possible time window whilst maintaining a consistent time series of mid-point dates (Table 1).

Identification of individual landslides was based on visual interpretation of true colour (R-G-B) and false colour (NIR) composites using bands 2-3-4-5 for Landsat 8 and 2-3-4-8 for Sentinel-2. Landslides were typically identified by the spectral contrast between exposed sediment or bedrock within the failure and the surrounding, undisturbed vegetation. Mapping of identified landslides in each epoch was conducted within QGIS v2.18 by two trained analysts using a 5 x 5 km fishnet grid to guide the mapping process. All landslides were manually digitised as vector polygons. The resolution of the satellite imagery meant that it was not possible to distinguish between failure source areas and deposits (cf. Roback et al., 2018). We characterised landslides by their planimetric area and by the ratio of area to perimeter (A/P), which indicates the degree of elongation; more elongate landslides have lower A/P values than those that are more equant. We did not convert area to volume due to uncertainties in both scaling laws (e.g., Larsen et al., 2010), potential aggregation of multiple polygons (e.g., Li et al., 2014; Marc and Hovius, 2015), and the wide variety of landslide types triggered by the event (Kargel et al., 2016).

Unlike previous multi-temporal inventory assessments (e.g., Fan et al., 2018; Fan et al., 2019; Li et al., 2018; Marc et al., 2019), we mapped the full extent of all landslides visible on imagery from each epoch, treating each epoch independently. This meant that we mapped landslides based solely on visibility in the imagery and irrespective of whether they had been documented during earlier epochs, rather than only recording landslides which had newly occurred or substantially changed since the preceding epoch. This approach was selected for a number of reasons. Focusing only on new landslides has the potential to underestimate any persistent hazard posed by previously failed slopes which have not yet fully stabilised or revegetated. In contrast, mapping all visible landslides from each epoch provides a measure of the total area of impacted ground for any given date, as well as allowing the overall rates of hillslope recovery and revegetation back to pre-earthquake levels to be derived. Understanding the degree to which the landslide hazard footprint persists or alters in the years following a large earthquake is crucial for determining a realistic measure of spatially- and temporally-variable hazard and risk. Our approach also avoids the need to classify the extent of reactivation of each landslide based on qualitative criteria (e.g., Li et al., 2018; Fan et al., 2018). With the medium-resolution imagery used here, it is not possible to observe variations in reactivation or remobilisation of debris within individual landslide scars. Thus, our

hillslope recovery rates (in terms of landslide areal density) are expected to be slower compared to studies that examine only new or clearly reactivated landslides in each epoch.

To assess the impact of this conceptual approach on our derived recovery rates, we have also applied an alternative methodology based on the analysis of individual 10 x 10 m cells rather than entire mapped polygons. In this approach, every 10 x 10 m cell within the study area was assigned a series of binary values showing whether it was a landslide ('1') or not ('0') within each of the mapping epochs. Cells that had been newly impacted relative to previous epochs, whether through the occurrence of entirely new landslides or expansion of existing landslide footprints, could then be isolated from persistent landslide cells and analysed separately in terms of their distribution and recovery rate. Additional information relating to this alternative methodology is provided in Supplementary Material 7, while a detailed consideration of the different conceptual approaches and the implications for assessing post-seismic hillslope recovery is discussed in Section 5.1.

Table 1. Landslide mapping epochs and dates

Epoch number	Epoch name	Acquisition date range	Interval (days)	Midpoint date	Sensor
1	Pre-monsoon 2014	02/04/2014 – 20/05/2014	48	26/04/2014	Landsat 8
2	Post-monsoon 2014	04/10/2014 – 30/11/2014	57	01/11/2014	Landsat 8
3	Pre-earthquake 2015	06/03/2015 – 22/03/2015	16	14/03/2015	Landsat 8
4	Coseismic 2015	30/04/2015 – 10/06/2015	41	20/05/2015	Landsat 8
5	Post-monsoon 2015	07/10/2015 – 17/11/2015	41	27/10/2015	Landsat 8
6	Pre-monsoon 2016	13/02/2016 – 26/04/2016	73	20/03/2016	Sentinel-2
7	Post-monsoon 2016	03/10/2016 – 29/12/2016	87	15/11/2016	Sentinel-2
8	Pre-monsoon 2017	07/02/2017 – 28/05/2017	110	03/04/2017	Sentinel-2
9	Post-monsoon 2017	04/11/2017 – 12/11/2017	8	08/11/2017	Sentinel-2
10	Pre-monsoon 2018	09/03/2018 – 08/05/2018	60	08/04/2018	Sentinel-2
11	Post-monsoon 2018	28/10/2018 – 30/10/2018	2	29/10/2018	Sentinel-2

A common issue with large-scale multi-temporal landslide inventory analysis is the presence of intermittent and spatially variable cloud, shadow, and snow cover, which typically precludes the direct comparison of data from affected areas. Automated masking of cloud, shadow, and snow cover was undertaken using the Fmask (Function of mask) software v4.0 (Qiu et al., 2019), with manual checking and editing of the resulting mask layers to ensure accuracy. Areas of persistent cloud or snow (i.e., those for which the ground was not visible in any of the eleven epochs) totalled 1,308.32 km^2, 5% of the total study area, and were

concentrated in the High Himalaya in the north of the study area. These areas were excluded from the analysis, leaving a 'seen ground' mapping extent of 24,266.68 km^2.

A second issue with multi-temporal inventories is intermittent visibility – that is, landslides which are visible in some epochs but obscured in others, due to cloud cover, shadowing, or poor image contrast. To address this issue, we developed a novel approach of forward propagation of landslide polygons from successive epochs based on a series of structured spatial overlap queries. Any landslides visible in both epoch *n*-1 and epoch *n*+1 that were obscured in epoch *n*, and that did not intersect a pre-existing epoch *n* polygon, were merged from epoch *n*-1 into the epoch *n* inventory. This process was extended to also extract landslides visible in epoch *n*-1 and epoch *n*+2 that were obscured in both epochs *n* and *n*+1. An additional spatial query identified landslides missed due to relief-based shadowing, a problem that was particularly acute on north-facing high-relief slopes in the study area. This involved selecting landslides from epoch *n*-1 that were within a one-pixel distance (with 15 m as the coarsest pixel resolution) of an epoch *n*+1 landslide but were more than one pixel distant from any landslide present in epoch *n*, and then merging these selected landslides into the epoch *n* inventory.

No landslides were propagated forward more than two epochs, equivalent to a maximum time interval of 12 months, and propagated landslides were tagged as inferred rather than directly mapped. Results were manually checked to ensure that the propagated landslides were correctly identified, and any erroneous polygons were removed. The number of landslides propagated forwards varied between epochs due to the differing extents and distributions of cloud and snow cover (Supplementary Material 1). An average of 940 landslides were propagated into each mapping epoch, representing a mean of 8% of each inventory. The maximum number of inferred landslides was for epoch 3 (pre-earthquake 2015) when cloud cover was highest, with 2,094 landslides being propagated from the two previous epochs. This equates to 33% of the epoch 3 inventory but this is proportionally higher than later epochs, due to the relatively low numbers of landslides in the pre-earthquake inventories.

3.2 Mapping uncertainties

Errors occur in all manually-mapped landslide inventories and relate to issues such as image clarity and the interpretative skills and experience of the mappers (Fan et al., 2018; Meena and Piralilou, 2019). Such errors were minimised for this study through (1) initial training of the mappers by repeat delineation of landslides within a 2,500 km^2 area that spanned a range of physiographic settings and landslide densities to identify and then correct individual mapper bias (see Supplementary Material 2), and (2) manual checking and editing of each completed inventory by a team of independent analysts. Each 5 x 5 km fishnet cell was assessed by a minimum of one mapper and by two independent analysts. This validation process involved the visual checking of each landslide polygon against the base imagery for that particular epoch. Landslides that had not been identified during the initial mapping were added and features that were determined to have been mistakenly mapped as landslides (such as quarries) were deleted from the inventory. Particular care was taken to ensure that any amalgamated landslides were segmented into individual polygons representing discrete failures, in order to provide accurate area-frequency distributions for each epoch (Marc and Hovius, 2015).

Direct comparisons were made between the coseismic inventory from this current study and that produced by Roback et al. (2018) using higher-resolution satellite imagery (Supplementary Material 3). We also quantified the influence of sensor type and spatial

resolution that might result from our two imagery types on landslide area characteristics through repeat mapping of a 121 km^2 subset area using a range of base imagery (Supplementary Material 4). This involved the repeat blind mapping of landslides visible on a Pleiades image tile from September 2015 (coincident with epoch 5) which had been resampled to different spatial resolutions (2 m, 10 m, 15 m), as well as equivalent mapping from a concurrent Landsat 8 tile which had been pan-sharpened to 15 m resolution.

3.3 Landslide area density analyses

Direct analysis of multi-temporal landslide polygon inventories is potentially complicated by small variations in polygon boundaries and overlaps between epochs, which can frustrate attempts to correlate polygons belonging to individual landslides. Without reliable correlation across epochs, it is difficult to establish the evolutionary trajectory of landsliding at a regional scale. An alternative means of monitoring temporal changes in landslide inventories is to divide the landscape into a grid of cells, and to consider the epochs in which cells first become affected by landsliding and then become inactive again once the hillslopes have healed and revegetated to the point that no potentially active landslides are visible. This framework can then be used to assess when each cell first and last experiences a landslide, the duration of activity, and the spatial extent of landslide activity at any given point in time.

We chose a cell size of 1 x 1 km as a compromise between retaining the spatial fidelity of the original mapped landslide inventories and detecting broad-scale spatio-temporal trends in landsliding across the entire affected area. For each cell, we assigned a value for (1) the first epoch in which that cell was intersected by one or more landslides, (2) the last epoch in which that cell was intersected, (3) the total number of epochs for which the cell was impacted by landsliding, and (4) the per-epoch landslide area density, expressed as a percentage of the cell area. These metrics enabled an assessment of the spatio-temporal variability in landslide area density and the distributions of density values recorded in our inventories, as well as providing insights into potential controls on the spatial distribution and timing of when particular cells became active (here termed the landslide ‘birth’ epoch) or inactive (the landslide ‘death’ epoch).

3.4 Physical controls on landsliding

A range of topographic and distance-based variables were summarised by individual landslide polygon and analysed for their potential influence on spatial and temporal variability in landslide birth and death. Kernel density estimations were generated for each variable and by each birth / death category, with the results then being differenced from equivalent density estimations for the overall study area.

Topographic information was sourced from the Advanced Land Observing Satellite (ALOS) World 3D – 30m (AW3D30) dataset, a freely-available global digital elevation model (DEM) at 30 m spatial resolution. Although slightly coarser than the mapping resolution, this DEM represents the highest-resolution openly available data with full coverage of the study area, and has been shown to be particularly suitable for modelling of topographic derivatives in mountainous terrain (Boulton and Stokes, 2018). We focused on derivatives that have previously been shown to relate to coseismic landsliding: slope, aspect, plan curvature, profile curvature, topographic wetness index, upslope contributing area, and hillslope relief (Parker et al., 2015; Robinson et al., 2017). The relative position of a landslide along the hillslope profile was calculated by measuring the minimum distance from the polygon perimeter to the nearest ridge top, to capture the position of the head scarp, and to the nearest river, to define the position of the toe. Distance values were then normalised to 0-1, with 0

representing the river and 1 the ridge. Earthquake-specific layers were also calculated, including distance to epicentre and slope direction to epicentre. The slope direction to epicentre was only calculated relative to the 25 April mainshock epicentre in Gorkha, rather than to both the mainshock and 12 May aftershock epicentres. This was because previous studies have demonstrated that the majority of landsliding associated with the Gorkha earthquake sequence was associated with the 25 April mainshock, with only a small number of new landslides triggered by the 12 May aftershock (Roback et al., 2018).

Rainfall data covering the study period were analysed to highlight any variation in precipitation trends that could potentially have contributed to temporal variability in landslide rates. Gridded monthly precipitation totals at a spatial resolution of 0.1° (11 x 11 km) were obtained from NASA's Global Precipitation Measurement (GPM) Integrated Multi-satellitE Retrievals for GPM (IMERG) dataset, covering the period from 2014 to 2018 (Supplementary Material 5). Individual NetCDF files were converted to geotiffs and then stacked to form a multiband raster containing 60 bands representing monthly precipitation totals. Mean monthly rainfall totals for the entire study area were then calculated by averaging the cell values from each raster band.

4. Results

The spatial pattern of landsliding in epoch 4 (coseismic) is shown in Fig. 1b, while the detailed temporal variability between inventories is shown in Fig. 1c for a small section of the study area. The full inventory includes 160,332 individually mapped landslide features across the 11 epochs. Inventory data for the whole area of interest are described in Fig. 2 and Table S1 in terms of number and area, and in Fig. 2a in terms of areal density, and relative to the timing and intensity of the monsoon in Fig. S8. Because of the complexity of these patterns, we focus first on aggregate statistical descriptions of our inventories, before turning to the distribution and evolution of landslide area density estimates.

4.1 Multi-temporal landslide inventory statistics

Landslide numbers are consistently low for each of the three pre-seismic inventories, averaging ~6,400, with little discernible difference between pre- and post-monsoon inventories (Fig. 2a). The 2015 Gorkha earthquake sequence (epoch 4) and 2015 monsoon (epoch 5) both led to substantial increases in the number of mapped landslides, with these inventories totalling 13,684 and 18,370 respectively. This number peaked at 18,978 in pre-monsoon 2016 (epoch 6), declined steadily through post-monsoon 2017 (epoch 9), and then increased again for pre- and post-monsoon 2018 (epochs 10 & 11). Importantly, by the end of the study period the number of visible landslides remained 4908 greater than were recorded in the coseismic inventory (13,684) and 12,193 greater than the pre-earthquake inventory average.

Total landslide area followed broadly the same pattern as landslide count, with consistency before the 2015 earthquake (mean = 64.63 km^2, σ = 1.71 km^2) and sharp increases immediately following the earthquake (154.68 km^2) and the 2015 monsoon (179.03 km^2) (Fig. 2a). Landslide area decreased steadily in 2016-17, albeit with pronounced fluctuations between pre- and post-monsoon epochs, with pre-monsoon inventories being ~22 km^2 (~16%) higher on average than their subsequent post-monsoon inventories. Whilst this appears large, this variability averages less than c. 30 m^2 / km^2 across our study area. In

contrast, areas in both pre- and post-monsoon 2018 inventories were similar, and still exceeded the area recorded by the immediate post-earthquake inventory (epoch 4).

The area-frequency distribution of landslides in the coseismic inventory is markedly different to the pre- and post-seismic inventories (Fig. 2b). Prior to the earthquake, the mean landslide area was ~10,000 m^2 with an A/P ratio of 14, and these values were relatively invariant across the three epochs. On average, coseismic landslides were both larger and less elongate than landslides before and after the earthquake, with a mean area of 11,300 m^2 and an area / perimeter (A/P) ratio of 15.3. Following the earthquake, both average area and A/P ratio declined through post-monsoon 2016 and then stabilised at values that were substantially lower than pre-earthquake levels – indicating a systematic shift to both smaller and more elongate failures than were observed before the earthquake.

Comparison with the independent inventory compiled by Roback et al. (2018) shows that our inventory contains fewer small landslides (areas $<10^3$ m^2) and an overall shift in the area distribution towards larger failures, consistent with our use of coarser resolution imagery (Supplementary Material 3; Fig. S4). Our coseismic inventory exhibits a characteristic probability density distribution with a rollover between 1,000 and 1,500 m^2 and power-law scaling with an exponent of 2.93 beyond a size threshold of 48,000 m^2 (Table S2). In comparison, the portion of the comparable inventory compiled by Roback et al. (2018) that overlaps with our study area has a rollover between 100 and 300 m^2 and a power-law exponent of 2.74 beyond a threshold area of 18,000 m^2. These differences are primarily due to the base imagery used for the mapping in each case, with our coseismic inventory being generated from 15 m resolution pan-sharpened Landsat 8 imagery, compared with the 0.2-0.5 m resolution Worldview imagery used by Roback et al. (2018). Repeat mapping of the 121 km^2 subset area outlined above (Section 3.2) shows a similar change in the probability density distributions when progressively coarsening image spatial resolution from 2 m to 15 m (Supplementary Material 4; Fig. S6). The overall distribution is shifted towards proportionally larger failures as image resolution is degraded and smaller failures become undetectable, with a corresponding increase in the average size of mapped landslides and decrease in the overall number of landslides in the inventory (Fig. S7). Power-law scaling of these subset inventories broadly indicates that the minimum landslide size threshold for the power-law fit increases as image resolution is degraded, although with pronounced variability which is likely the result of a relatively small mapping area and inventory sample size (Table S3).

4.2 Evolution of landslide area density distribution

When averaged using a 1 x 1 km grid, the overall landslide area density increased markedly as a result of the earthquake. The per-epoch mean area density followed the same pattern as total landslide area: increasing to 0.62% after the earthquake and 0.72% after the 2015 monsoon, declining through 2016-17, and remaining higher than the coseismic value after the 2018 monsoon (Fig. 2a). The spatial distribution of landslide area density provides a useful visualisation of the pattern of pre-seismic, coseismic, and post-seismic landsliding (Fig. 3a). The landscape-scale impact of the earthquake is clearly visible as a widespread increase in landslide area density at epoch 4 across the entire study area, focused in particular along a broad northwest-southeast band following the physiographic divide between the Lesser Himalaya / Middle Hills and the High Himalaya (Fig. 3a). In each of the pre-earthquake epochs, 15% of grid cells within the study area were impacted by landslides, increasing to 24% following the earthquake then to 29% following the 2015 monsoon (Fig. 3b). The

proportion of cells impacted by landslides then stayed high (28-30%) for the remainder of the time series.

Pairwise differencing between individual epochs shows that changes in the spatial pattern of landslide density through time were highly spatially correlated (Fig. 4a). The change between pre-seismic and coseismic inventories (epochs 3-4) clearly shows the focusing of landslide activity within the major valleys draining the High Himalaya, particularly within Gorkha, Sindupalchok, Rasuwa, Dhading, and Dolakha districts (see Fig. 1 for district names). Between the earthquake and the 2015 monsoon (epochs 4-5) there was a systematic shift in landslides towards the higher-elevation regions of the northerly districts of the study area. Within those areas, however, there were also clusters of reduced landslide density, with more areas experiencing a reduction in landslide density (16% of the study area) than an increase (13%) between post-monsoon 2015 and pre-monsoon 2016 (Fig. 4b). As expected from the temporal changes in landslide area (Fig. 2), area densities tended to decrease during subsequent monsoons and increase between the end of one monsoon and the start of the next. In epochs 9-10 and 10-11, we observe secondary increases in landslide density through the central and north-central parts of the study area, including the northern part of Kabhrepalanchok district – well outside of the main northwest-southeast band of intense landsliding.

Overall, landslide area density across much of the area was still markedly higher in post-monsoon 2018 than it was immediately prior to the 2015 earthquake, especially within the major river valleys that flow from the High Himalaya (Fig. 5a). Over 25% of the study area had an increased density relative to pre-earthquake conditions, compared with only 7% with a decreased density (Fig. 5c). When compared to the coseismic landslide pattern, the post-seismic pattern of change, up to and including post-monsoon 2018, is more spatially complex (Fig. 5b), with approximately the same proportion of cells having experienced increased (19%) and decreased (16%) landslide densities (Fig. 5c). Much of the central northwest-southeast band of intense coseismic landsliding experienced a decrease in density over this time period, with the greatest changes concentrated on the lower slopes of major river valleys. At the same time, there are substantial zones of increased post-seismic landsliding in western Sindhupalchok and northern Nuwakot, as well as the higher ground across the northern margin of the study area. A more dispersed area of increased landslide density is also present within the Lesser Himalaya in the southeast of the study area, stretching across Okhaldunga, Ramechhap and northern Sindhuli districts (Fig. 5b). Qualitative observations from districts recording pronounced post-seismic changes demonstrate a range of commonly-observed behaviours, including the occurrence of new post-seismic landslides, expansion of pre-existing landslides through both retrogression and downslope channelised runout, and recovery of coseismic landslide scars; some of these behaviours can be seen in the detailed changes visible in Fig. 1c.

4.3 Spatial and temporal distribution of landslide birth and death

Categorising grid cells by landslide ‘birth’ and ‘death’ results in nine discrete classes (Fig. 6). For example, there were three classes associated with landslides that were triggered by the 2015 earthquake (‘coseismic birth’), distinguished based on whether the landslides were no longer visible after the coseismic inventory (‘coseismic death’), disappeared during one of the post-seismic epochs (‘pre-2018 monsoon death’) or were still visible in the final mapping epoch (‘post-2018 monsoon survival’). The distribution of these classes is spatially correlated, with clustering of areas that have recovered since the earthquake and those where

new post-earthquake landslides have occurred (Fig. 6a). Grid cells in which the landslide hazard persisted to the end of the study period – that is, areas where landslides were still visible in the post-monsoon 2018 inventory - dominate the distribution. Those cells where landslides were born before the earthquake are distributed throughout the study area, although somewhat clustered in the high-relief areas to the north and also the foothills to the south and east of the Kathmandu valley. In contrast, cells where landslides were born during the earthquake are largely restricted to the main northwest-southeast band of intense landsliding between the two epicentres. Cells where landslides were born after the earthquake are particularly concentrated in the valleys peripheral to the coseismic distribution, with a notable shift northward towards areas of higher elevation and the upstream reaches of the drainage network.

To assess the extent of clustering, we considered cells in each category in turn, and examined the distribution of categories within the eight cells adjacent to each cell. Clustering is noticeably greater for the three classes containing landslides which persisted to the end of the study period than for those which recovered before that time (Fig. 6b). For example, 34% of cells adjacent to those which were activated in the earthquake and which still contained mapped landslides in post-monsoon 2018 are from the same class, compared with only 21% for cells which were coseismically activated but which had recovered prior to post-monsoon 2018. In general terms, cells which recovered at any point during the time series were more spatially isolated and tended to occur around the periphery of clusters of cells containing persistent landsliding.

More grid cells were initially activated during the three pre-earthquake mapping epochs (17% of the total number) than were activated by the earthquake (9%). Importantly, this observation indicates that, although the density of landsliding caused by the earthquake was much higher (Fig. 3), the spatial area impacted was comparatively confined (Fig. 6c). The persistence of both pre-earthquake and coseismic landsliding through time is clear, as 81% of the cells activated prior to the earthquake and 77% of the cells activated during the earthquake still contained landslides by post-monsoon 2018. Of the total population of cells, 13% were first impacted by landsliding during a post-earthquake epoch, with 73% of these still containing one or more landslides by post-monsoon 2018.

For the majority of epochs, the proportion of grid cells newly affected relative to the preceding epoch was low (1-2%), with the exception of the earthquake (10%), the 2015 monsoon (6%) and pre-monsoon 2018 (3%) (Fig. 6d). About 11% of grid squares in the post-monsoon 2018 epoch had been newly affected relative to the earthquake distribution, indicating that the spatial pattern of landsliding had altered steadily but progressively since the earthquake.

4.4 Topographic controls on regional-scale landslide birth and death

Of the ten topographic derivatives tested, four variables showed clear skill in explaining landslide birth and death: elevation, slope angle, slope direction to epicentre, and normalised distance from river to ridgeline. The other topographic variables showed either no consistent relationships or no clear difference between birth and death epochs and so were omitted from further analysis. We focus here on understanding potential controls on patterns of landslide activation and recovery post-earthquake, and we note that more detailed analysis of the controls on landsliding within individual inventories can be found elsewhere (e.g., Martha et al., 2017; Roback et al., 2018).

4.4.1 Elevation

Landslides within grid cells that were first activated during pre-earthquake epochs preferentially occurred at elevations between 2500 and 5000 m, representing the elevation range of the intermediate hillslopes covering much of the High Himalaya to the north of the study area (Fig. 7a). In contrast, the distribution of coseismically-activated cells was shifted towards lower elevations between 1500 and 4000 m. This corresponds with the band of intense seismic shaking caused by the 2015 earthquake and correlates with other studies of the coseismic inventory (e.g., Roback et al., 2018). The elevation distribution for landslides occurring within cells that were first activated after the earthquake shows a shift back towards higher elevations, with a modal peak in the density difference at 3000 m. This shift towards higher elevations is also reflected in the northward movement of high post-seismic landslide area density (Figs. 4-6). In all three birth categories, landslides occurred much less often at lower (<1500 m) and higher (>5000 m) elevation ranges. For context, 46% of the mapping area has an elevation <1500 m and 8% of the area has an elevation >5000 m.

Elevation is also correlated with the timing of grid cell recovery (Fig. 7b). Landslides within cells that recovered prior to the earthquake tended to preferentially occur within elevations between 1500 and 4500 m. This is lower than the range for pre-earthquake birth cells, suggesting that lower-elevation locations were more likely to recover. Locations which recovered after the earthquake were similarly shifted towards lower elevations, likely reflecting the elevation range at which most coseismic landslides occurred. The coseismic landslide death distribution (i.e., landslides that disappeared between the coseismic 2015 and post-monsoon 2015 epochs) is peaked at higher elevations of 3000-4500 m, albeit with a small sample size (n = 117 cells) compared with the other classes. Cells in which landslide activity persisted through the end of the study period typically occurred at higher elevations (mostly >2500 m), again indicating that hillslopes at higher elevations are recovering more slowly.

4.4.2 Slope angle

The influence of slope angle on landslide birth and death also differs between categories. Landslides within grid cells with a pre-earthquake landslide birth preferentially occurred on slopes of between 30 and 55°, with a modal peak of 40° (Fig. 7c). The coseismic birth distribution was shifted toward noticeably higher slope angles, occurring more commonly than would otherwise be expected between 35 and 65° and with a pronounced peak at 45°. Landslides in cells activated after the earthquake showed a partial return to pre-seismic conditions. Locations which recovered prior to the earthquake were typically within the same range of slope values as those where pre-seismic landslides had occurred, 30-55° (Fig. 7d). Locations which recovered after the earthquake broadly reflect the slope distribution of coseismic births, but with a shift towards slightly lower slopes. In contrast, the distribution for cells in which landsliding persisted beyond post-monsoon 2018 was offset towards higher slope angles and with a peak at 42°, indicating that landslides on steeper hillslopes were generally more likely to persist whereas those on shallower slopes were likely to recover more quickly. Cells which recovered during the coseismic inventory show a very different distribution, with a peak at much lower slope angles (20°), but this curve is again defined by a relatively small sample size.

4.4.3 Slope direction to epicentre

Slope direction relative to the Gorkha earthquake epicentre is defined so that 0° represents hillslopes that directly face the epicentre, 90° represents those perpendicular, and 180° represents those that face directly away from the epicentre. Pronounced asymmetry in the density of landslides due to slope direction relative to the seismic source has been previously demonstrated for coseismic landslide inventories (Robinson et al., 2017), due to localised variability in topographic amplification of seismic waves (Meunier et al., 2008). The distribution of values for grid cells that were activated during and after the earthquake shows that landslides occurred preferentially on hillslopes facing away from the epicentre (90-175°) (Fig. 7e). The pre-earthquake distribution also shows, however, that landslides occurred preferentially at these slope direction values. Since this distribution is entirely independent of the direction of seismic shaking, the pattern is likely to instead be related to the direction of prevailing monsoonal rains in the region, which typically originate from the south-southeast and which may therefore preferentially impact upon south-facing hillslopes with relative slope directions of 90-180°.

The pre-earthquake and coseismic landslide death distributions show that hillslopes approximately perpendicular to the epicentre (75-150°) were more likely to recover than those facing more directly towards or away from the epicentre (Fig. 7f). Again, because the pre-earthquake distribution is independent of the earthquake, this likely reflects the aspects on which most rainfall-triggered landslides occurred, and may also indicate that hillslopes directly facing the direction of monsoonal rains were less likely to recover than those which were partially sheltered. In contrast, grid cells which recovered after the earthquake as well as those that persisted beyond post-monsoon 2018 broadly reflect the equivalent birth distributions. This again suggests that, for this particular earthquake and study area, the slopes most affected by the earthquake are also those which are most susceptible to rainfall-triggered landsliding due to the predominant direction of monsoonal rains.

4.4.4 Normalised distance from river to ridgeline

Landslides are often observed to occur more frequently towards the top and bottom of a normalised hillslope profile. Seismic shaking is amplified by topography, triggering a concentration in landsliding near ridge tops (Meunier et al., 2008). In contrast, locations close to a river can also result in larger landslide frequencies due to high pore fluid pressure and undercutting of hillslopes (Densmore and Hovius, 2000). Landslides in grid cells activated prior to the Gorkha earthquake showed a clear tendency towards lower hillslope positions close to rivers and were under-represented towards ridge tops (Fig. 7g). In contrast, coseismic landslides occurred more uniformly along the entire hillslope profile, with the exception of the extreme ridge top locations. Landslides in cells activated after the earthquake show a similar distribution to the coseismic inventory, although shifted slightly towards the pre-seismic pattern.

Although pre-earthquake landslides were more likely to occur at lower hillslope positions, landslides within cells which recovered prior to the earthquake were typically at mid-slope locations (Fig. 7h). Landslides within cells which recovered after the earthquake broadly followed the coseismic and post-seismic birth distributions. Landslides in cells which had not recovered by post-monsoon 2018, however, show a clear tendency towards lower hillslope positions close to the river network. This persistent activity may be due to fluvial undercutting of hillslopes (Cook et al., 2018) or downslope movement of landslide material by debris flows (Dahlquist and West, 2019; Tian et al., 2020).

5. Discussion

Our results provide the first comprehensive, regional-scale demonstration of how the pattern of landsliding has varied in the years after a large continental earthquake. While our findings agree in some ways with the understanding gained from studies of previous earthquakes, there are also some important differences – most notably, our observation that the number and area of potentially active landslides remained high through the first 3.5 years after the earthquake, and were nowhere close to recovering to pre-earthquake levels. Our study also documents systematic and profound shifts in the pattern of landslide activity over time, both during and after the earthquake, and at both the regional scale and the scale of individual hillslopes. Below, we discuss the spatio-temporal evolution of landsliding in more detail and speculate on some potential controls behind the patterns that we observe, before considering the implications of our results for post-earthquake hazard, response, and reconstruction efforts.

5.1 Spatiotemporal evolution of post-seismic landsliding

5.1.1 Conceptual approach

Determining the rate of landscape recovery after a large earthquake depends fundamentally on (1) the definition of recovery and (2) the data that are used to assess it. Most previous multi-temporal inventory studies have tended to focus on either the occurrence of new landslides (e.g., Marc et al., 2015, 2019) or new landslides plus visible reactivation of coseismic landslides (e.g., Li et al., 2018; Fan et al., 2018) to define the rate of post-seismic landsliding; the temporal decay of this rate to pre-earthquake levels is then used as a proxy for recovery to assumed pre-earthquake conditions of hillslope stability (e.g., Marc et al., 2015). While this approach accurately characterises the susceptibility of the landscape to new failures, it will underestimate the hazard posed by coseismic and post-seismic landslides as long as those failures are persistent within the landscape – that is, as long as they continue to move and supply sediment to downslope areas. The widespread occurrence of debris flows after large earthquakes (e.g., Zhang and Zhang, 2017; Dahlquist and West, 2019) illustrates the ease with which landslide debris may be remobilised from pre-existing failures. Some studies have attempted to address this shortcoming with qualitative estimates of reactivation or remobilisation (e.g., Li et al., 2018; Fan et al., 2018). In the absence of intensive field monitoring, however, this determination is challenging, even with high-resolution imagery; furthermore, neither field monitoring nor the acquisition and analysis of high-resolution imagery are yet feasible over the scale of the entire rupture area in a large continental earthquake. An exclusive focus on new landsliding also implicitly assumes that revegetation happens rapidly enough to stabilise existing failures and impede the further transport of debris downslope. A growing number of studies have now demonstrated that the link between revegetation and reduced failure rates after the Wenchuan earthquake is complex (e.g., Yang et al., 2017; Yang et al., 2018; Shen et al., 2020), with both spatial and temporal variations in vegetation regrowth and landslide occurrence (Ni et al., 2019). This complexity is to be expected from the diverse mechanical and hydrological ways in which vegetation affects shallow hillslope stability, especially in a landscape recently impacted by an earthquake (e.g., Stokes et al., 2014; Cohen and Schwarz, 2017).

In contrast, by mapping each epoch independently, our approach implicitly assumes that, to first order, landslide activity is only effectively impeded once bare earth is no longer visible in the medium-resolution imagery. Until that point, we assume that the landslide can potentially undergo continued failure or remobilisation of landslide debris and can continue to supply sediment to downslope areas. This is clearly also an oversimplification of recovery – not least because the point at which bare earth is no longer visible will depend upon the specific sensor, band combination, and spatial resolution that are used. By employing Landsat 8 and Sentinel-2 data throughout our study, we have sought to minimise these variations across the different epochs. The trade-off with this approach is a decreased ability to resolve both the smallest failures (Figs. S4 and S6) and the extent of continued activity or remobilisation within existing failures (e.g., Fan et al., 2018). Our approach therefore provides a precautionary view of the potential hazard posed by existing landslides, due to the over-estimation of the time period over which they may remain active, but we suggest this as a more defensible approach when assessing risk. In sum, both approaches have advantages and disadvantages, and it is critical to bear their differences in mind when considering the results of any multi-temporal analysis. These differences point to the need to better understand the detailed biophysical relationships between what is visible in imagery, and how vegetation recovery and mass wasting evolve in the aftermath of a large earthquake.

5.1.2 Temporal variability in landslide rates

Our results demonstrate that both the number of landslides and the total landslide area remained well above coseismic levels to the end of 2018, approximately 3.5 years after the Gorkha earthquake (Fig. 2). This indicates that the recovery period when measured in terms of the number and extent of persistent and therefore potentially active landslides present within the landscape is considerably longer than initial estimates suggested (e.g., Marc et al., 2019), and is instead likely to be on the order of 10 years or more. We note that studies which mapped all visible failures in the years after the Wenchuan (e.g., Huang and Li, 2014; Li et al., 2018; Tang et al., 2016, Chen et al., 2020) and Kashmir (Shafique, 2020) earthquakes have also inferred decade-scale recovery times.

Our results do match the rapid recovery inferred by other studies, however, in terms of a return to pre-earthquake landslide and debris flow rates within 1-2 years (Dahlquist and West, 2019; Marc et al., 2019), when we focus only on the changing number of newly impacted 1 km^2 grid cells (Fig. 6d) or the landslide birth rate based on individual 100 m^2 landslide cells (Supplementary Material 7). Analysing the multi-temporal inventory data in this way indicates that the number of new landslide cells remained high in post-monsoon 2015 but then declined rapidly, with the post-monsoon 2018 level being only marginally higher than that for the post-monsoon 2014 inventory (Fig. S11). The difference in per-epoch landslide cell birth and death counts is even more pronounced, with the net change indicating that more landslide cells were disappearing than being newly created by the pre-monsoon 2016 epoch. This suggests that, when measured simply in terms of the occurrence of new landslide activity, the recovery rate following the earthquake was comparable to that obtained from previous studies that have taken a similar methodological approach, with the landscape returning close to pre-earthquake levels within just a few years. Importantly, however, this approach overlooks the persistence of existing landslide scars within the landscape, as illustrated by the high number of cells which were still mapped as landslides in post-monsoon 2018.

While the spatial and temporal patterns of post-earthquake recovery revealed by our data are highly complex, there is evidence for distinct clustering and evolution of landslide activity after the earthquake (Fig. 6). The complexity of the changes that we describe reflects the numerous landslide types and sizes triggered by the earthquake (Kargel et al., 2016), which are likely to each change through time in a different manner. It is therefore reasonable to assume that the recovery of each landslide reflects both failure mechanism and setting, and so exploring recovery as a function of landslide type or mechanism would be desirable. Whilst the nature of coseismic landslides is to some extent controlled by conditions at the time of the earthquake (Roback et al., 2018), the degree to which sediment production from coseismic landslides is fully accomplished during initial shaking must also define the future potential for continued landsliding in the period that follows (Marc et al., 2015). It is widely understood that some coseismic landslide types are more sensitive to reactivation under rainfall (e.g., as debris flows), but equally that some evolve via mechanisms that have a more complex relationship with controlling conditions and hence time. This includes, for example, progressive landslides initiated by the earthquake (Terzaghi, 1950), which are likely to exhibit some independence from environmental forcing and so remain difficult to associate with characteristic timescales of recovery beyond those set by site-specific conditions.

Interestingly, there remains only limited forensic research on how landslide failure mechanism or the evolution of hillslope-scale rock strength influences the trajectory of post-seismic recovery (e.g., Chen et al., 2020), beyond the exhaustion of supply to debris flows (e.g., Dalquist and West, 2019). Whilst some form of asymptotic decay describing the reduction in intensity of many post-seismic landsliding processes seems appropriate as, for example, material supply is exhausted, for others the actual nature of change is likely to be quite different in form, which may be reflected in the landscape-scale patterns that we report. For example, we note an incremental post-seismic shift to failures at higher elevation which may tentatively reflect a retrogressive mode of landslide change, which is only mechanically possible for some types of landslide in some positions in the landscape. We also note that some mapped processes, such as landslide runout and scarp stabilisation, may act to cancel each other out in aggregated statistics, and so are not captured in averaged measures of landslide activity. Therefore, without a single dominant coseismic landslide type, it remains to be shown how such mechanism-dependent timescales interleave, and at what scale these can be summarised into a single event ‘recovery’ timescale. New post-seismic landslides are one relatively well-constrained component of this wider range of processes, but again that approach commonly aggregates landslides driven by a number of failure mechanisms. It is clear that a fuller understanding of post-earthquake landsliding needs to unpick how these various landslide types and mechanisms evolve and recover.

We have not converted total landslide area to volume because of uncertainty relating to scaling relationships (e.g., Li et al., 2014) as well as potential amalgamation of landslide areas (Marc and Hovius, 2015) that cannot be resolved with our medium-resolution imagery. Nonetheless, the persistence of large areas of potentially active landsliding across the study area through to the end of the post-monsoon 2018 period is consistent with, although not conclusive proof of, the continued presence of large amounts of coseismic and post-seismic landslide debris. We tentatively infer from this observation that much of this material is therefore still sequestered within the landscape. Similarly, Huang and Li (2014) documented that 80-90% of erodible material remained on hillslopes five years after the Wenchuan earthquake, while Fan et al. (2018) suggested that more than 90% of the coseismic landslide debris produced during the Wenchuan earthquake was still contained on hillslopes and in low-order channels after seven years.

Somewhat surprisingly, our results show slightly higher total landslide areas for the pre-monsoon inventories in 2016 and 2017, compared to their post-monsoon equivalents (Fig. 2). All else being equal, we would expect the monsoon both to trigger new landslides and to reactivate existing landslides, leading to higher total post-monsoon areas. Close examination of the inventories suggests, however, that this counter-intuitive result may be due at least in part to the visibility of landslide outlines under post-monsoon vegetation conditions, relative to pre-monsoon conditions (Fig. 8). Ground visibility is greater in our medium-resolution imagery in pre-monsoon imagery, whereas landslide boundaries in the post-monsoon mapping periods are partly obscured by overhanging vegetation. This leads to persistent decreases in the mapped extent of post-monsoon landslides compared to their pre-monsoon equivalents. In support of this observation, we note that the area distributions for the pre-monsoon 2016 and 2017 inventories are shifted toward larger areas relative to the post-monsoon inventories (Fig. 2b), but that the number of mapped landslides does not show the same fluctuation (Fig. 1a). Comparable seasonal variability has been noted in multi-inventory landslide studies that analyse vegetation recovery (e.g., Yang et al., 2018; Ni et al., 2019), but our results indicate that these phenological variations may also be important for inventories created from manual mapping of optical imagery. Importantly, the observed cyclicity in pre- and post-monsoon landslide area totals does not appear to correlate with inter-annual variability in monsoon rainfall totals (Fig. S8), and remains small in proportion to the wider longer-term changes that we observe. Our results do, however, highlight a potential uncertainty in single epoch inventories, or single inventories that are mapped from imagery that spans multiple vegetation seasons.

5.1.3 Spatial distribution of landslides

Our area density results indicate that, even at the resolution of our approach (1 km^2), there is clear and consistent evidence for both reactivation of existing pre-seismic and coseismic landslides and new post-seismic landsliding. Overall, the most intense areas of landslide activity appear to have migrated northward, from a northwest-southeast belt of intense coseismic activity to lower-order parts of the regional-scale drainage network by the end of the study period (Fig. 5). We also observe an overall shift in activity up and away from trunk streams toward higher parts of the landscape (Fig. 7a), with clear reductions in landslide density on the lower slopes of the major N – S river valleys through Gorkha, Rasuwa, Dhading, Sindhupalchok and Dolakha districts.

Somewhat paradoxically, this large-scale shift in the locus of landslide activity occurs at the same time that debris from existing pre-seismic and (especially) coseismic landslides is remobilised and transported downslope and into the drainage network (Fig. 1c). Changes in area-perimeter ratios through time show increasing elongation of landslide form between the earthquake and post-monsoon 2016, followed by a reduction in elongation through 2018 (Fig. 2b). By the end of the study period the area-perimeter ratio was still well below the average levels from the three pre-earthquake inventories, likely indicating widespread progressive runout and remobilisation of coseismic failures in the years after the earthquake. This remobilisation has led to persistent disruption to infrastructure, particularly the highway network, as documented by Tian et al. (2020). It is important to distinguish these distinct patterns of migration from each other, as they are occurring at different scales, and again may otherwise cancel out in wider scale averaged measures of change. We note as well that our ability to assess remobilisation and downslope transport is almost certainly limited by the constrained widths of landslide and debris-flow deposits within the confines of the channel

network, especially given the resolution of our imagery and concealment by vegetation at lower elevations. Thus, our estimates of downslope runout and landslide elongation must be taken as minima.

It would be reasonable to expect that the spatial footprint of landsliding triggered by the 2015 earthquake might evolve with time to one more characteristic of monsoon-triggered landsliding. By the end of the study, the area of the landscape that exceeded pre-earthquake landslide densities remained largely coincident with the full coseismic landslide footprint (Figs. 4a and 5a), rather than being concentrated around the areas with the highest coseismic landslide densities.The implication is that even after 3.5 years, a wide area remained subject to continued landslide hazard, and thus that at the event scale coseismic landslide density alone is a poor predictor of the potential for persistent landsliding in the post-earthquake period. In other words, persistent landsliding should be expected anywhere within the affected area, not just in the areas with highest coseismic lansldide density. Within the overall affected area, the spatial changes in landslide distribution through time are not random, and show clear patterns in terms of which areas have recovered since the earthquake and which have not (Fig. 6). Clustering was greater for areas with landslides which persisted until the end of the study period than for those which recovered prior to that time, with the latter tending to be more spatially isolated and located around the periphery of clusters containing persistent landslides (Fig. 6a-b).

An important outcome of our study is the recognition of substantial new post-seismic landsliding, occurring in areas that did not fail during the earthquake. Almost 10% of cells across the study area show post-seismic onset of landsliding that persisted through the end of the 2018 monsoon (Fig. 6c). The clustering of these areas indicates that at this scale, the location of coseismic landsliding is not necessarily a good predictor of the location of post-seismic landsliding, which raises important considerations for hazard assessment. We note specifically that, had we chosen to focus on a smaller study area, recognition of this pattern would have been considerably more difficult. In future large continental earthquakes, it is therefore important to establish the overall spatio-temporal distribution of landsliding, rather than making wider inferences based on small subsets of the affected area.

5.2 Controls on the evolution of co- and post-seismic landsliding

The systematic spatial evolution of co- and post-seismic landsliding after the 2015 Gorkha earthquake suggests that there are some underlying physical controls on the locations that are most susceptible to reactivation and continued activity, as well as those that have recovered. Understanding these controls is critical to our ability to anticipate how landslide hazard is likely to change after a future event. Here, we compare our results to inferences from previous large continental earthquakes.

Stark spatial variations in the speed of recovery have been noted following the 2005 Kashmir and 2008 Wenchuan earthquakes (e.g., Khan et al., 2013; Ni et al., 2019; Shafique, 2020; Shen et al., 2020), but to our knowledge our study is the first to demonstrate this effect over (nearly) the entire earthquake-affected area. A number of studies have tried to link these variations to elevation, slope angle, or aspect. For example, Khan et al. (2013) argued that landsliding rates stabilised within the first few years after the Kashmir earthquake, and that sites at lower elevations recovered faster in terms of the regrowth of vegetation and inferred cessation of activity. We observe qualitatively similar shifts after the Gorkha earthquake, although the lack of spatio-temporal information in Khan et al. (2013) means that we cannot

directly compare the spatial patterns observed in Nepal (Figs. 3-4) with those in Kashmir. Similarly, both Fan et al. (2018) and Yunus et al. (2020) observed that post-seismic landslides after the 2008 Wenchuan earthquake were more likely to occur at higher elevations, a trend that Yunus et al. (2020) linked to slower rates of vegetation recovery in those locations. In contrast, Li et al. (2018) argued that new landslides in part of the Wenchuan earthquake-affected area occurred preferentially at lower elevations except during periods of high rainfall; they tentatively linked this preference to river erosion and human activities, and distinguished between new landsliding and the progressive shift of coseismic landslide debris toward lower parts of the landscape. At present, we do not know whether the progressive shift in landslide activity toward the headwater reaches of the drainage network after Gorkha, as visible in Fig. 5b, reflects large-scale vegetation change, or is due to another mechanism, such as the subsequent failure of hillslopes that were damaged in the earthquake but did not fully collapse (cf. Dadson et al., 2004), large-scale retrogression of failure upslope from existing landslide locations, or some other cause. Investigation of this spatial shift is a priority for future research.

Slope angle and aspect have also been invoked in disparate ways to explain landslide patterns after past earthquakes. Fan et al. (2018) argued that post-seismic landsliding typically occurred on lower slope angles, reflecting remobilisation of landslide debris within the channel network – a pattern also noted by Hovius et al. (2011), who showed that the locus of landslide activity migrated to lower hillslope positions over time after the 1999 Chi-Chi earthquake. In contrast, both Li et al. (2018) and Yunus et al. (2020) documented a shift in new landslides toward progressively higher slope angles, a trend that Yunus et al. (2020) linked to slower revegetation on those hillslopes. Our results provide evidence of a return in post-seismic landsliding toward similar slope angle values to those that were active before the earthquake (Fig. 7c), as well as continued persistence of landslide activity at the highest slope values in the landscape (Fig. 7d). In terms of aspect, Fan et al. (2018) showed that post-seismic landslides typically occurred on the same southeast-facing hillslopes as the coseismic inventory. They suggested that this could be due to both climatic factors as well as the distribution of earthquake damage. This similarity is broadly reflected in our results, which demonstrate coseismic and post-seismic landsliding on hillslopes with common orientations (Fig. 7e). Conversely, Yunus et al. (2020) showed that west- and northwest-facing hillslopes, in the shadow of the regional monsoon wind direction, had fewer landslides but also recovered more slowly than hillslopes at other aspects.

A number of prior studies have also linked post-seismic landslide persistence to human activities, including road-building, construction, terracing and other agricultural activities, and mining (e.g., Khan et al., 2013; Li et al., 2018). Anecdotal observations from the Gorkha earthquake show that comparable links are likely to have been present in Nepal as well. This is an important phenomenon, not least because reconstruction activities are likely to be focused in the first few years after a large earthquake when landslide rates also remain high. Similarly, it is highly likely that (re)construction on ground damaged by the earthquake, or in areas always previously considered safe, will be far more challenging. Some of the post-seismic increases in landslide density within the Lesser Himalaya and south of Kathmandu (Fig. 5b) correspond directly to major road corridors, and are almost certainly indicative of failures along either these corridors or along lesser branch roads, visible even at the regional scale.

Landslides associated with the construction of new rural roads are visible in our medium-resolution imagery (Fig. 9), particularly in the pre- and post-monsoon 2018 inventories. This

uptick tallies with the proliferation of rural road construction associated with the set-up of the new federal structure of government in Nepal in 2017 (Sudmeier-Rieux et al., 2019). We are not aware of any systematic attempt to document the growth of the rural road network in Nepal or its links to persistent post-earthquake landslide activity, and this remains another priority for future research. It may be the case that post-seismic landsliding will not return to pre-earthquake levels in locations undergoing widescale infrastructure development due to the consequent impacts on the landscape.

5.3 Implications for recovery and reconstruction following a large earthquake

It is common that the scientific effort focussed on understanding catastrophic earthquakes is poorly aligned with decision making and information needs on the ground (Williams et al. 2018; Datta et al. 2018). A key challenge relates to providing timely information on the likely future dynamics of landsliding triggered by earthquakes in a timeframe that dovetails with response and reconstruction. In this context, the rate and pattern of landslide activity and landscape recovery after a large earthquake are a first-order control on long-term seismic hazard, and so both synoptic and site-specific knowledge of what is likely to occur are highly valuable for both recovery and reconstruction, and future preparedness planning. We have documented the persistence of large areas of potentially active landsliding across the entire Gorkha earthquake-affected area, even after 3.5 years, indicating that hillslopes have not recovered as rapidly as might be inferred by studies that focus only on new failures (e.g., Marc et al., 2019). Our data also illustrate that, importantly, the nature of landslide hazard and therefore risk can significantly change through time after an earthquake. Our mapping illustrates that landslides triggered on the day of the earthquake, or even in the first few years after the earthquake, can evolve in terms of location. This dynamic risk must be reflected in messaging for earthquake-affected populations, and recovery and reconstruction efforts need to be cognisant of the potential continued changes that the landscape might experience. Our approach is in part intended to inform this type of effort in future and to feed into risk sensitive planning that accounts for rainfall- and earthquake-triggered landslide risk (e.g., Milledge et al., 2019), as well as the processes that play out in the aftermath of a large earthquake. Our approach provides a more conservative view of the persistence of landslide activity than earlier studies, which is arguably more appropriate in guiding risk averse planning that must also recognise people's everyday livelihood concerns and wider systemic risks (Oven et al., in press). While there is an understandable desire to rebuild, doing so too quickly and ignoring the risk of post-seismic landsliding and remobilised landslide debris can have devastating impacts on people, their homes, and infrastructure.

Our results demonstrate three key messages for dynamic landslide hazard. First, for the study area as a whole, coseismic landslide occurrence – but not landslide density – is a reasonable first-order guide to the locations of persistent post-seismic landsliding over the 3.5 years of our study period (Fig. 6c-d). Second, the coseismic landslide pattern cannot capture the nearly 10% of cells that show new and persistent post-earthquake landsliding – so the coseismic pattern should not simply be projected forward in time to anticipate the evolution of the hazard. Finally, the spatial clustering observed in our data means that areas of post-earthquake landslide activity should be expected to persist, all else being equal. These findings are useful for triaging areas of greatest risk in the immediate aftermath of a large earthquake, and for highlighting the manner in which landslide hazard is likely to evolve as disaster response and reconstruction progresses. More locally, one important caution illustrated by the dynamic nature of the hazard is that cultural memory or experience of living with landslide risk in these regions developed prior to a large earthquake may be less relevant

in dealing with coseismic and post-seismic landsliding in the years after an earthquake (Alexander, 2000).

We see several promising ways in which our multi-temporal inventories could be used in order to provide a better assessment of future landslide hazard across the Gorkha earthquake-affected area in Nepal. The first relates to providing a regional-scale understanding of the continued evolution of landslide activity, as coseismic and post-seismic landslide debris is remobilised and as existing landslide complexes evolve, with a view to informing ongoing recovery and reconstruction (Fig. 1c). Further analysis would require physically-based modelling of the release, entrainment and transport of landslide debris (e.g., Croissant et al., 2019), perhaps embedded within a wider consideration of the earthquake-triggered hazard chain (e.g., Fan et al., 2019). Second, our inventories could be used to tune regional-scale post-earthquake landslide susceptibility models, in order to improve their skill in anticipating the occurrence of new failures relative to static models that do not account for the Gorkha earthquake. Finally, our data provide an assessment of the trajectory of stability for individual landslides, which adds considerably to static one-off site assessments, providing insight for ongoing mitigation of landslide risk in this region of Nepal. This is relevant to the National Reconstruction Authority's on-going National Geohazards Assessment, which seeks to support landslide-affected communities following the 2015 earthquake.

6. Conclusions

We have systematically mapped pre-, co-, and post-seismic landslides across the 14 administrative districts of Nepal that were most intensively affected by the 2015 Gorkha earthquake, covering about 90% of the total area affected by coseismic landsliding and continuing until the end of the 2018 monsoon. This represents, to our knowledge, the first systematic multi-temporal landslide inventory that spans nearly the entire rupture area of a large continental earthquake across both the earthquake itself and the following four monsoon seasons. Our mapping documents a sharp increase in both number and area of landslides caused by the earthquake, and further increases after the first post-earthquake monsoon in 2015. The numbers and total area of mapped landslides have fluctuated in the following years, with greater areas in the pre-monsoon inventories – likely due to seasonal changes in vegetation and visibility of landslide margins. Nevertheless, both landslide number and area remained greater than the coseismic inventory at the end of this study period, indicating a high degree of persistent and evolving landslide activity. It is therefore important to recognise that landslide hazard remains significant several years after this earthquake.

Coseismic landsliding was concentrated in a northwest-southeast band along the physiographic divide between the Lesser and Higher Himalaya. In general, coseismic landslides were larger on average than those that occurred before the earthquake, and they occurred at lower elevations, on steeper slopes, and higher up on individual hillslope profiles. The years immediately after the earthquake have seen the continued evolution of landsliding across the whole impacted area, rather than a progressive constriction around the most severely impacted locations. We see clear evidence that post-seismic landslide activity has shifted northwards, higher in the drainage network, although there is also some evidence of recovery to pre-earthquake patterns in terms of slope gradients and hillslope positions. This northward shift is superimposed upon a smaller-scale change in the pattern of landslide activity, as pre- and coseismic landslide material has been remobilised and transported downslope into the drainage network. We also see substantial evidence of post-seismic

landsliding in areas that were not badly affected by coseismic impacts, both in the far northern margins of the rupture area and within parts of the Lesser Himalaya.

When amalgamated into landslide area density estimates on a 1 km^2 spatial grid, our results indicate that most areas of high landslide activity have persisted throughout the study period, irrespective of whether activity started before or during the earthquake. These areas of persistent activity are highly spatially correlated and are somewhat predictable on the basis of simple topographic metrics, which is important for understanding the temporal evolution of landslide hazard. We see evidence of local systematic shifts in landsliding, with notable reductions in landsliding in the lower slopes of major river valleys over time, and a tendency for spatial clustering of specific landslide evolution trajectories. Further studies of post-earthquake landslide hazard could focus on the continued remobilisation and transport of existing landslide debris, or on the ways in which our inventories can be used to constrain changes in landslide susceptibility.

Our study takes a distinct conceptual approach in mapping all visible areas of disturbance during each epoch, rather than concentrating solely on the occurrence of new landslides. We demonstrate that unpacking landsliding after an earthquake in this manner reveals a wide variety of mass wasting processes that may each follow a different trajectory to recovery, so that recovery warrants both careful definition and choice of how it is described. This methodology assesses directly the time period over which an existing landslide may remain active, and thus yields a more precautionary approach to generating information about hazards that is suitable for understanding the regional-scale development of landsliding.

Acknowledgements

This research has been supported by the UKRI-DFID SHEAR program (201844-112). We recognise the contributions of a wider group of analysts from Durham University who fed into various stages of the mapping campaign since 2015, post-mapping support from D Hodgson, N Cox, G Basyal, R Shrestha and M Brain, and discussions around the development of the mapping data with MR Dhital, TN Bhattarai, and C Shrestha. We also thank colleagues at NSET (SN Shrestha, G Jimee), and DFID (T Sumner and S Dugar). L Goren, G Bennett and one anonymous reviewer provided valuable comments that have helped to improve the manuscript. Landslide area density data are freely available from https://doi.org/10.5281/zenodo.4274486.

Contributions

The research was enabled by funding from UKRI-DFID SHEAR to NJR. The ideas were jointly developed by all authors in discussion with friends and colleagues in Nepal. Landslide mapping was undertaken by RS and DPS as part of a wider effort to increase capacity in landslide risk assessment in Nepal. Data analysis and interpretation was undertaken by MEK, NJR, TRR and ALD. The manuscript was written by MEK, NJR, ALD and TRR, with input from all other authors.

References

Alexander, D., 2000. *Confronting catastrophe: new perspectives on natural disasters*. Oxford University Press, USA.

Alstott, J., Bullmore, E. and Plenz, D. 2014. Powerlaw: a Python package for analysis of heavy-tailed distributions. PLoS ONE 9(1): e85777. https://doi.org/10.1371/journal.pone.0085777

Avouac, J.P., Meng, L., Wei, S., Wang, T. and Ampuero, J.P., 2015. Lower edge of locked Main Himalayan Thrust unzipped by the 2015 Gorkha earthquake. *Nature Geoscience*, 8(9), pp.708-711. https://doi.org/10.1038/ngeo2518

Aydin, N.Y., Duzgun, H.S., Heinimann, H.R., Wenzel, F. and Gnyawali, K.R., 2018. Framework for improving the resilience and recovery of transportation networks under geohazard risks. *International Journal of Disaster Risk Reduction*, 31, pp.832-843. https://doi.org/10.1016/j.ijdrr.2018.07.022

Barth, S., Geertsema, M., Bevington, A.R., Bird, A.L., Clague, J.J., Millard, T., Bobrowsky, P.T., Hasler, A. and Liu, H., 2019. Landslide response to the 27 October 2012 earthquake (M_w 7.8), southern Haida Gwaii, British Columbia, Canada. *Landslides*, pp.1-10. https://doi.org/10.1007/s10346-019-01292-7

Bernard, T. G., Lague, D., and Steer, P. In Review, 2020. Beyond 2D inventories : synoptic 3D landslide volume calculation from repeat LiDAR data, *Earth Surface Dynamics Discussion*. https://doi.org/10.5194/esurf-2020-73

Bird J.F. and Bommer, J.J., 2004. Earthquake losses due to ground failure. *Engineering Geology*, 75(2), pp. 147-179. https://doi.org/10.1016/j.enggeo.2004.05.006

Boulton, S.J. and Stokes, M., 2018. Which DEM is best for analyzing fluvial landscape development in mountainous terrains? *Geomorphology*, 310, pp.168-187. https://doi.org/10.1016/j.geomorph.2018.03.002

Budimir, M.E.A., Atkinson, P.M. and Lewis, H.G., 2014. Earthquake-and-landslide events are associated with more fatalities than earthquakes alone. *Natural Hazards*, 72(2), pp.895-914. https://doi.org/10.1007/s11069-014-1044-4

Chen, M., Tang, C., Xiong, J., Shi, Q.Y., Li, N., Gong, L.F., Wang, X.D. and Tie, Y., 2020. The long-term evolution of landslide activity near the epicentral area of the 2008 Wenchuan earthquake in China. *Geomorphology*, 367. https://doi.org/10.1016/j.geomorph.2020.107317

Clauset, A., Rohilla Shalizi, C. and Newman, M.E.J. 2009. Power-Law distributions in empirical data. SIAM Review, 51(4), 661-703. https://doi.org/10.1137/070710111

Cohen, D. and Schwarz, M., 2017. Tree-root control of shallow landslides. *Earth Surface Dynamics*, 5, pp. 451-477. https://doi.org/10.5194/esurf-5-451-2017

Cook, K.L., Andermann, C., Gimbert, F., Adhikari, B.R. and Hovius, N., 2018. Glacial lake outburst floods as drivers of fluvial erosion in the Himalaya. *Science*, 362(6410), pp.53-57. https://doi.org/10.1126/science.aat4981

Croissant, T., Steer, P., Lague, D., Davy, P., Jeandet, L., and Hilton, R.G., 2019. Seismic cycles, earthquakes, landslides and sediment fluxes: Linking tectonics to surface processes using a reduced-complexity model. *Geomorphology*, 339, pp.87-103. https://doi.org/10.1016/j.geomorph.2019.04.017

Dadson, S.J., Hovius, N., Chen, H., Dade, W.B., Lin, J.C., Hsu, M.L., Lin, C.W., Horng, M.J., Chen, T.C., Milliman, J. and Stark, C.P., 2004. Earthquake-triggered increase in sediment delivery from an active mountain belt. *Geology*, 32(8), pp.733-736. https://doi.org/10.1130/G20639.1

Dahlquist, M.P. and West, A.J., 2019. Initiation and runout of post-seismic debris flows: Insights from the 2015 Gorkha Earthquake. *Geophysical Research Letters*, 46, pp.9658-9668. https://doi.org/10.1029/2019GL083548

Dai, F.C., Xu, C., Yao, X., Xu, L., Tu, X.B. and Gong, Q.M., 2011. Spatial distribution of landslides triggered by the 2008 Ms 8.0 Wenchuan earthquake, China. *Journal of Asian Earth Sciences*, 40(4), pp.883-895. https://doi.org/10.1016/j.jseaes.2010.04.010

Datta, A., Sigdel, S., Oven, K., Rosser, N., Densmore, A. and Rijal, S., 2018. The role of scientific evidence during the 2015 Nepal earthquake relief efforts. Overseas Development Institute (ODI) Report. ODI, London. Available from: https://www.odi.org/publications/11044-role-scientific-evidence-during-2015-nepal-earthquake-relief-efforts

Densmore, A.L. and Hovius, N., 2000. Topographic fingerprints of bedrock landslides. *Geology*, 38(4), pp.371-374. https://doi.org/10.1130/0091-7613(2000)28%3C371:TFOBL%3E2.0.CO;2

Fan, X., Domènech, G., Scaringi, G., Huang, R., Xu, Q., Hales, T.C., Dai, L., Yang, Q. and Francis, O., 2018. Spatio-temporal evolution of mass wasting after the 2008 M w 7.9 Wenchuan earthquake revealed by a detailed multi-temporal inventory. *Landslides*, 15(12), pp.2325-2341. https://doi.org/10.1007/s10346-018-1054-5

Fan, X., Scaringi, G., Domènech, G., Yang, F., Guo, X., Dai, L., He, C., Xu, Q. and Huang, R., 2019. Two multi-temporal datasets that track the enhanced landsliding after the 2008 Wenchuan earthquake. *Earth System Science Data*, 11(1), pp.35-55. https://doi.org/10.5194/essd-11-35-2019

Fan, X., Scaringi, G., Korup, O., West, A.J., van Westen, C.J., Tanyas, H., Hovius, N., Hales, T.C., Jibson, R.W., Allstadt, K.E. and Zhang, L., 2019. Earthquake-induced chains of geologic hazards: Patterns, mechanisms, and impacts. *Reviews of Geophysics*, 57(2), pp.421-503. https://doi.org/10.1029/2018RG000626

Hovius, N., Meunier, P., Lin, C.W., Chen, H., Chen, Y.G., Dadson, S., Horng, M.J. and Lines, M., 2011. Prolonged seismically induced erosion and the mass balance of a large

earthquake. *Earth and Planetary Science Letters*, *304*(3-4), pp.347-355. https://doi.org/10.1016/j.epsl.2011.02.005

Huang, R. and Li, W., 2014. Post-earthquake landsliding and long-term impacts in the Wenchuan earthquake area, China. *Engineering Geology*, 182, pp.111-120. https://doi.org/10.1016/j.enggeo.2014.07.008

Huang, M.Y.F. and Montgomery, D.R., 2012. Fluvial response to rapid episodic erosion by earthquake and typhoons, Tachia River, central Taiwan. *Geomorphology*, 175, pp.126-138. https://doi.org/10.1016/j.geomorph.2012.07.004

Kargel, J.S., Leonard, G.J., Shugar, D.H., Haritashya, U.K., Bevington, A., Fielding, E.J., Fujita, K., Geertsema, M., Miles, E.S., Steiner, J. and Anderson, E., 2016. Geomorphic and geologic controls of geohazards induced by Nepal's 2015 Gorkha earthquake. *Science*, 351(6269), p.aac8353. https://doi.org/10.1126/science.aac8353

Khan, S.F., Kamp, U. and Owen, L.A., 2013. Documenting five years of landsliding after the 2005 Kashmir earthquake, using repeat photography. *Geomorphology*, 197, pp.45-55. https://doi.org/10.1016/j.geomorph.2013.04.033

Larsen, I., Montgomery, D. and Korup, O., 2010. Landslide erosion controlled by hillslope material. *Nature Geoscience*, 3, pp.247-251. https://doi.org/10.1038/ngeo776

Li, G., West, A.J., Densmore, A.L., Jin, Z., Parker, R.N. and Hilton, R.G., 2014. Seismic mountain building: Landslides associated with the 2008 Wenchuan earthquake in the context of a generalized model for earthquake volume balance. *Geochemistry, Geophysics, Geosystems*, 15(4), pp.833-844. https://doi.org/10.1002/2013GC005067

Li, C., Wang, M. and Liu, K., 2018. A decadal evolution of landslides and debris flows after the Wenchuan earthquake. *Geomorphology*, 323, pp.1-12. https://doi.org/10.1016/j.geomorph.2018.09.010

Marc, O. and Hovius, N., 2015. Amalgamation in landslide maps: effects and automatic detection. *Natural Hazards and Earth System Sciences*, 15(4), pp.723-733. https://doi.org/10.5194/nhess-15-723-2015

Marc, O., Hovius, N., Meunier, P., Uchida, T. and Hayashi, S., 2015. Transient changes of landslide rates after earthquakes. *Geology*, 43(10), pp.883-886. https://doi.org/10.1130/G36961.1

Marc, O., Behling, R., Andermann, C., Turowski, J.M., Illien, L., Roessner, S. and Hovius, N., 2019. Long-term erosion of the Nepal Himalayas by bedrock landsliding: the role of monsoons, earthquakes and giant landslides. *Earth Surface Dynamics*, 7(1), pp.107-128. https://doi.org/10.5194/esurf-7-107-2019

Martha, T.R., Roy, P., Mazumdar, R., Govindharaj, K.B. and Kumar, K.V., 2017. Spatial characteristics of landslides triggered by the 2015 Mw 7.8 (Gorkha) and Mw 7.3 (Dolakha) earthquakes in Nepal. *Landslides*, 14(2), pp.697-704. https://doi.org/10.1007/s10346-016-0763-x

Meena, S.R. and Tavakkoli Piralilou, S., 2019. Comparison of Earthquake-Triggered Landslide Inventories: A Case Study of the 2015 Gorkha Earthquake, Nepal. *Geosciences*, 9(10), pp.437-454. https://doi.org/10.3390/geosciences9100437

Meunier, P., Hovius, N. and Haines, J.A., 2008. Topographic site effects and the location of earthquake induced landslides. *Earth and Planetary Science Letters*, 275(3-4), pp.221-232. https://doi.org/10.1016/j.epsl.2008.07.020

Milledge, D.G., Densmore, A.L., Bellugi, D., Rosser, N.J., Watt, J., Li, G., and Oven, K.J., 2019. Simple rules to minimise exposure to coseismic landslide hazard. *Natural Hazards and Earth System Scien*ces, 19, 837–856. https://doi.org/10.5194/nhess-19-837-2019

Ni, Z., Yang, Z., Li, W., Zhao, Y. and He, Z., 2019. Decreasing trend of geohazards induced by the 2008 Wenchuan earthquake inferred from time series NDVI data. *Remote Sensing*, 11(19), p.2192-2222. https://doi.org/10.3390/rs11192192

Oven, K., Rana, S., Basyal, G.K., Rosser, N. and Kincey, M. (in press) Policies, Politics and Practices of Landslide Risk Management in Post-Earthquake Nepal: Perspectives from Above and Below. In Hutt, M., Leichty, M., and Lotter, S. (Eds.) Epicentre to Aftermath: Rebuilding and Remembering in the Wake of Nepal's Earthquakes. Delhi: Cambridge University Press.

Parker, R.N., Hancox, G.T., Petley, D.N., Massey, C.I., Densmore, A.L. and Rosser, N.J., 2015. Spatial distributions of earthquake-induced landslides and hillslope preconditioning in northwest South Island, New Zealand. *Earth Surface Dynamics.* 3(4), pp.501-525. https://doi.org/10.5194/esurf-3-501-2015

Qiu, S., Zhu, Z. and He, B., 2019. Fmask 4.0: Improved cloud and cloud shadow detection in Landsats 4–8 and Sentinel-2 imagery. *Remote Sensing of Environment*, 231, pp.111-205. https://doi.org/10.1016/j.rse.2019.05.024

Roback, K., Clark, M.K., West, A.J., Zekkos, D., Li, G., Gallen, S.F., Chamlagain, D. and Godt, J.W., 2018. The size, distribution, and mobility of landslides caused by the 2015 M_w 7.8 Gorkha earthquake, Nepal. *Geomorphology*, 301, pp.121-138. https://doi.org/10.1016/j.geomorph.2017.01.030

Robinson, T.R., Rosser, N.J., Densmore, A.L., Williams, J.G., Kincey, M.E., Benjamin, J. and Bell, H.J., 2017. Rapid post-earthquake modelling of coseismic landslide magnitude and distribution for emergency response decision support. *Natural Hazards and Earth System Sciences*, 17, pp.1521-1540. https://doi.org/10.5194/nhess-17-1521-2017

Shafique, M., 2020. Spatial and temporal evolution of co-seismic landslides after the 2005 Kashmir earthquake. *Geomorphology*, 362. https://doi.org/10.1016/j.geomorph.2020.107228

Shen, P., Zhang, L.M., Fan, R.L., Zhu, H. and Zhang, S. 2020. Declining geohazard activity with vegetation recovery during first ten years after the 2008 Wenchuan earthquake. *Geomorphology*, 352. https://doi.org/10.1016/j.geomorph.2019. 106989

Stokes, A., Douglas, G.B., Fourcaud, T., Giadrossich, F., Gillies, C., Hubble, T., Kim, J.H., Loades, K.W., Mao, Z., McIvor, I.R., Mickovski, S.B., Mitchell, S., Osman, N., Phillips, C., Poesen, J., Polster, D., Preti, F., Raymond, P., Rey, F., Schwarz, M. and Walker, L.R., 2014.

Ecological mitigation of hillslope instability: ten key issues facing researchers and practitioners. *Plant Soil*, 377, pp. 1-23. https://doi.org/10.1007/s11104-014-2044-6

Sudmeier-Rieux, K., Devkota, S., Rajbhandari, P.C.L., Howell, J. and Sharma, S., 2019. Invited perspectives: Mountain roads in Nepal at a new crossroads. *Natural Hazards and Earth System Sciences,* 19(3), pp.655-660. https://doi.org/10.5194/nhess-19-655-2019

Tang, C., Van Westen, C.J., Tanyas, H. and Jetten, V.G., 2016. Analysing post-earthquake landslide activity using multi-temporal landslide inventories near the epicentral area of the 2008 Wenchuan earthquake. *Natural Hazards and Earth System Sciences,* 16(12), pp.2641-2655. https://doi.org/10.5194/nhess-16-2641-2016

Tanyaş, H., Van Westen, C.J., Allstadt, K.E., Anna Nowicki Jessee, M., Görüm, T., Jibson, R.W., Godt, J.W., Sato, H.P., Schmitt, R.G., Marc, O. and Hovius, N., 2017. Presentation and analysis of a worldwide database of earthquake-induced landslide inventories. *Journal of Geophysical Research: Earth Surface,* 122(10), pp.1991-2015. https://doi.org/10.1002/2017JF004236

Terzaghi, K., 1950. Mechanism of landslides. In S Paige (Ed.), *Application of Geology to Engineering Practice*. Geological Society of America, New York, pp. 83-123.

Tian, Y., Owen, L.A., Xu, C., Ma, S., Li, K., Xu, X., Figueiredo, P.M., Kang, W., Guo, P., Wang, S., Liang, X. and Maharjan, S.B., 2020. Landslide development within 3 years after the 2015 M_w 7.8 Gorkha earthquake, Nepal. *Landslides*, 17, pp.1251-1267. https://doi.org/10.1007/s10346-020-01366-x

Tiwari, B., Ajmera, B. and Dhital, S., 2017. Characteristics of moderate-to large-scale landslides triggered by the M_w 7.8 2015 Gorkha earthquake and its aftershocks. *Landslides*, 14(4), pp.1297-1318. https://doi.org/10.1007/s10346-016-0789-0

Wang, J., Jin, Z., Hilton, R.G., Zhang, F., Densmore, A.L., Li, G. and West, A.J., 2015. Controls on fluvial evacuation of sediment from earthquake-triggered landslides. *Geology*, *43*(2), pp.115-118. https://doi.org/10.1130/G36157.1

Weiss, D.J. and Walsh, S.J., 2009. Remote Sensing of Mountain Environments. *Geography Compass*, 3(1), pp.1-21. https://doi.org/10.1111/j.1749-8198.2008.00200.x

Williams, J.G., Rosser, N.J., Kincey, M.E., Benjamin, J., Oven, K.J., Densmore, A.L., Milledge, D.G., Robinson, T.R., Jordan, C.A. and Dijkstra, T.A., 2018. Satellite-based emergency mapping using optical imagery: experience and reflections from the 2015 Nepal earthquakes. *Natural Hazards and Earth System Sciences*, 18, pp.185-205. https://doi.org/10.5194/nhess-18-185-2018

Xu, C., Xu, X., Yao, X. and Dai, F., 2014. Three (nearly) complete inventories of landslides triggered by the May 12, 2008 Wenchuan Mw 7.9 earthquake of China and their spatial distribution statistical analysis. *Landslides*, *11*(3), pp.441-461. https://doi.org/10.1007/s10346-013-0404-6

Xu, C., Xu, X., Tian, Y., Shen, L., Yao, Q., Huang, X., Ma, J., Chen, X. and Ma, S., 2016. Two comparable earthquakes produced greatly different coseismic landslides: The 2015

Gorkha, Nepal and 2008 Wenchuan, China events. *Journal of Earth Science*, 27(6), pp.1008-1015. https://doi.org/10.1007/s12583-016-0684-6

Yang, W., Qi, W., Wang, M., Zhang, J. and Zhang, Y., 2017. Spatial and temporal analyses of post-seismic landslide changes near the epicentre of the Wenchuan earthquake. *Geomorphology*, 276, pp.8-15. https://doi.org/10.1016/j.geomorph.2016.10.010

Yang, W., Qi, W. and Zhou, J., 2018. Decreased post-seismic landslides linked to vegetation recovery after the 2008 Wenchuan earthquake. *Ecological Indicators*, 89, pp.438-444. https://doi.org/10.1016/j.ecolind.2017.12.006

Yunus, A.P., Fan, X., Tang, X., Jie, D., Xu, Q. and Huang, R., 2020. Decadal vegetation succession from MODIS reveals the spatio-temporal evolution of post-seismic landsliding after the 2008 Wenchuan earthquake. *Remote Sensing of Environment*, 236, p.111476. https://doi.org/10.1016/j.rse.2019.111476

Zhang, S. and Zhang, L.M., 2017. Impact of the 2008 Wenchuan earthquake in China on subsequent long-term debris flow activities in the epicentral area. *Geomorphology*, 276, pp.86-103. https://doi.org/10.1016/j.geomorph.2016.10.009

Zhang, Jin, Z., West, A.J., An, Z., Hilton, R.G., Wang, J., Li, G., Densmore, A.L., Yu, J., Qiang, X., Sun, Y., Li, L., Gou, L., Xu, Y., Xu, X., Liu, X., Pan, Y. and You, C.F., 2019. Monsoonal control on a delayed response of sedimentation to the 2008 Wenchuan earthquake. *Science Advances*, 5. https://doi.org/10.1126/sciadv.aav7110

FIGURES

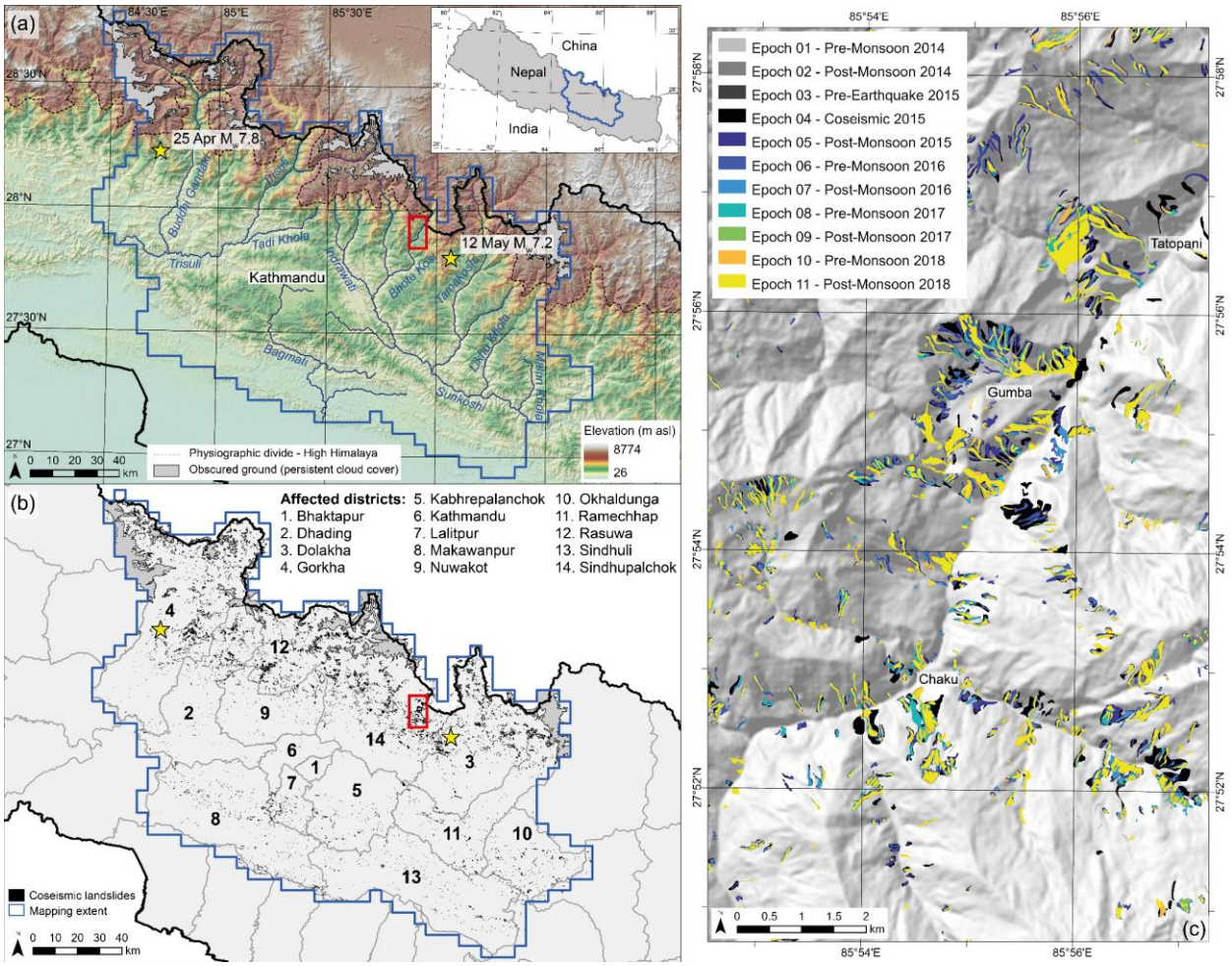

Figure 1. Location of the study area in central Nepal. (a) Shaded relief elevation map derived from a 30-m ALOS DEM of the study area (Credit: AW3D30 – JAXA). Stars show the main epicentres of the 2015 Gorkha earthquake sequence: 25 April M_w 7.8 and 12 May M_w 7.2. Grey polygons show areas of persistent cloud or snow cover throughout the study period, which were excluded from the analysis. Red box shows location of panel (c). (b) Spatial distribution of coseismic landslides (epoch 4) mapped across the 14 administrative districts that were most intensively affected by the earthquake. (c) Example of multi-temporal landslide inventory results for an area of the upper Bhote Kosi river basin in Sindhupalchok. Note complex patterns of overlap between polygons from different inventories; this complicates spatial correlation and analysis of regional-scale evolutionary patterns, and motivates our focus on area density estimates.

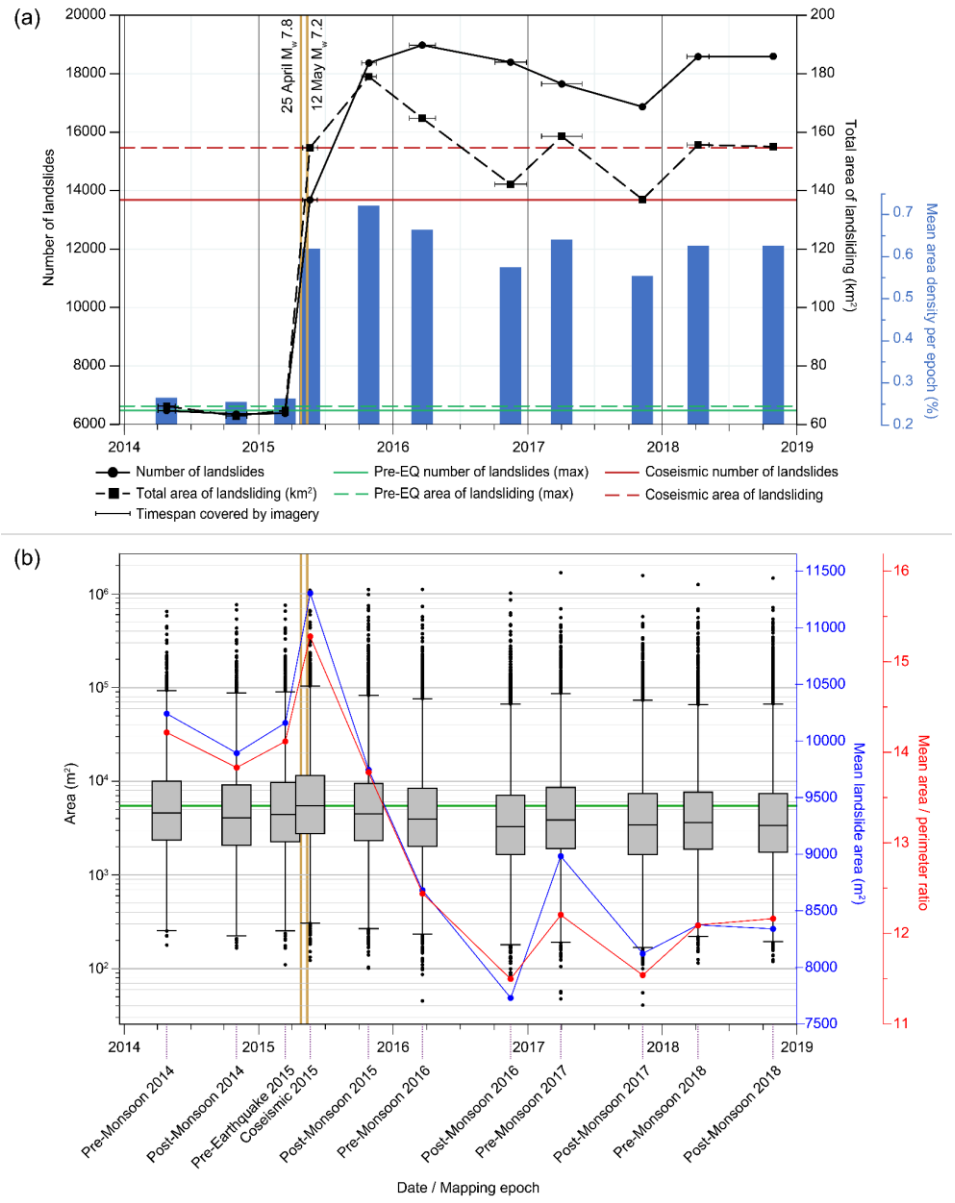

Figure 2. Summary statistics derived from the 2014-2018 multi-temporal landslide inventories. (a) Landslide count and area statistics for the eleven mapping epochs. Horizontal bars on each data point represent the timespan covered by the satellite imagery used for the mapping. Maximum pre-earthquake landslide number and area are shown by the green horizontal lines, with coseismic number and area shown by the red horizontal lines. Blue bars indicate the mean landslide area density per epoch based on a 1 km^2 fishnet grid covering the mapped extent. Vertical orange lines indicate the dates of the 25 April M_w 7.8 Gorkha earthquake and the 12 May M_w 7.2 aftershock. (b) Landslide area change through time, shown as box plots including area data from all mapped polygons, and the mean landslide area and mean area / perimeter ratio for each mapping epoch. Horizontal lines on boxes represent the median value, grey boxes show the interquartile range (IQR), and the whiskers define all data within 1.5 IQR of the nearer quartile. Data points beyond 1.5 IQR are shown individually. The horizontal green line shows the median landslide area for the coseismic inventory (epoch 4). The differences between the mean and median values highlight the skew in the size distribution of the inventories. High mean area / perimeter ratio values indicate more compact, rounded shapes; lower ratio values indicate greater elongation.

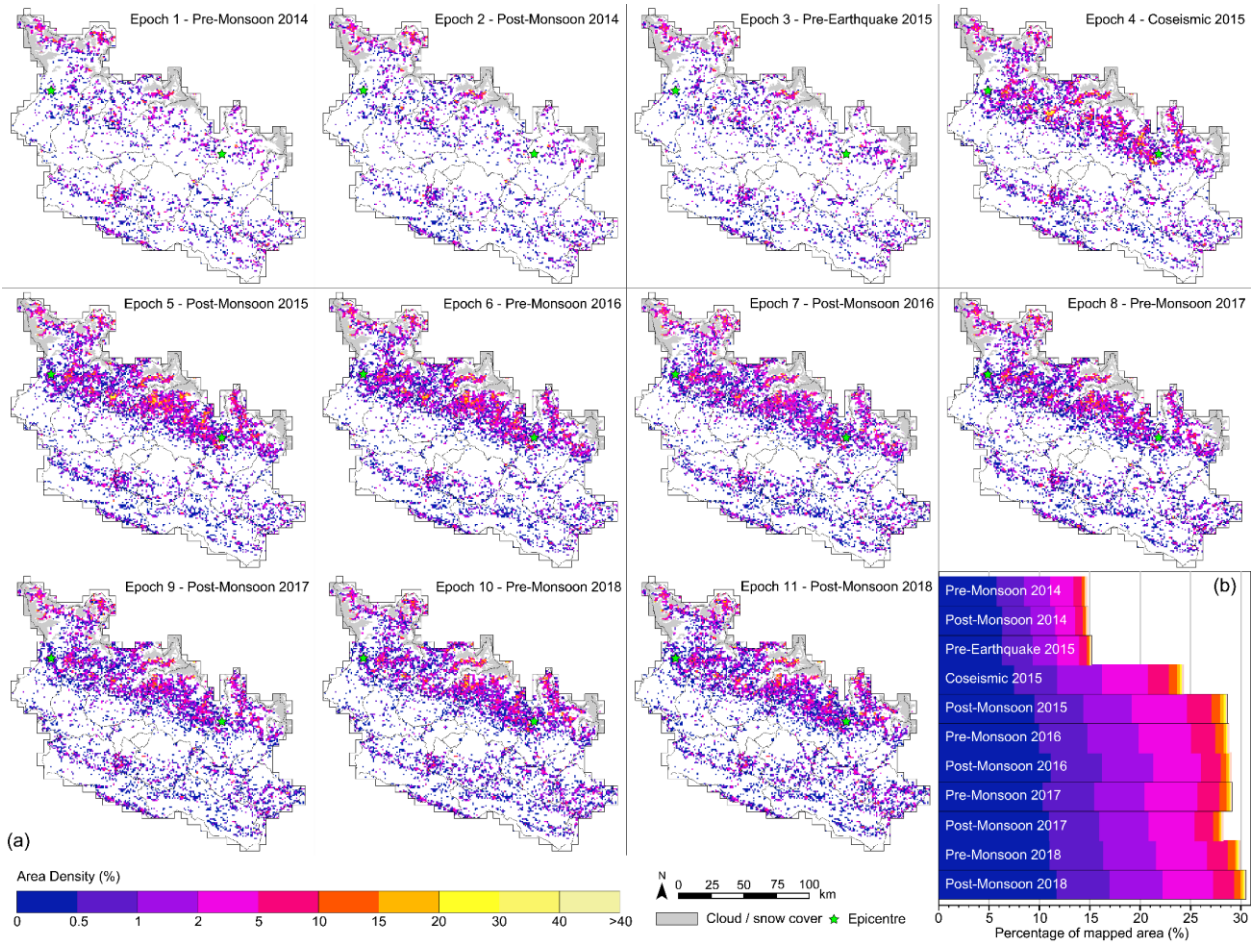

Figure 3. (a) Landslide area density for each of the 11 mapping epochs. Density values are expressed as a percentage of each 1 km2 grid cell. Grey polygons show areas of persistent cloud or snow cover which were excluded from the analysis. (b) Distribution of area density values within each mapping epoch, using the same colour scale.

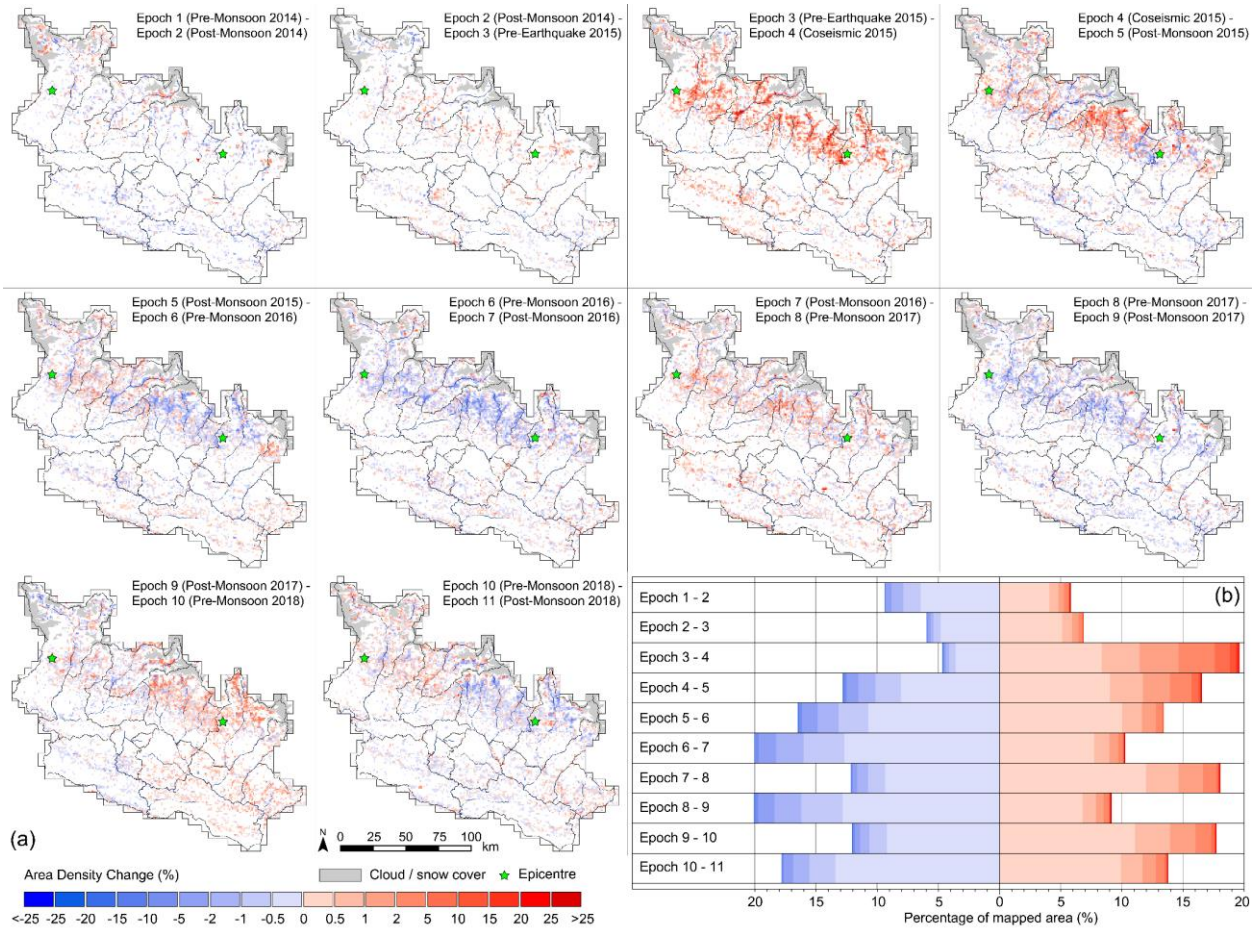

Figure 4. (a) Landslide area density change between pairwise mapping epochs. Data are shown as change in landslide area density as a percentage of each 1 km2 grid cell, with red colours indicating an increase in area density and blue colours a decrease. Grey polygons show areas of persistent cloud or snow cover which were excluded from the analysis. (b) Distribution of change values for all cells across each successive pair of epochs, using the same colour scale.

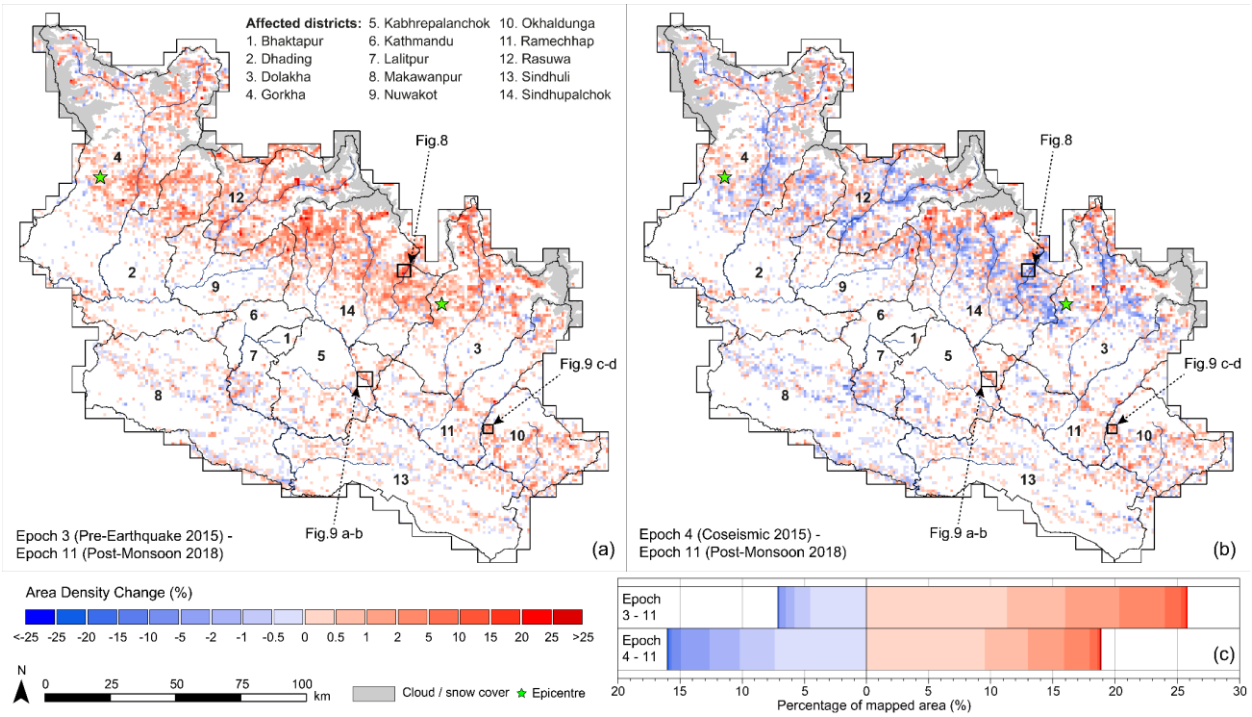

Figure 5. Landslide area density change between (a) the pre-earthquake 2015 and post-monsoon 2018 landslide inventories and (b) the coseismic 2015 and post-monsoon 2018 landslide inventories. Change in landslide area density is shown as a percentage of each 1 km^2 grid cell, with red colours indicating an increase in area density and blue colours a decrease. Grey polygons show areas of persistent cloud or snow cover which were excluded from the analysis. Black inset boxes mark the locations of detail images shown in Figures 8 and 9. (c) Distribution of change values for all cells, using the same colour scale.

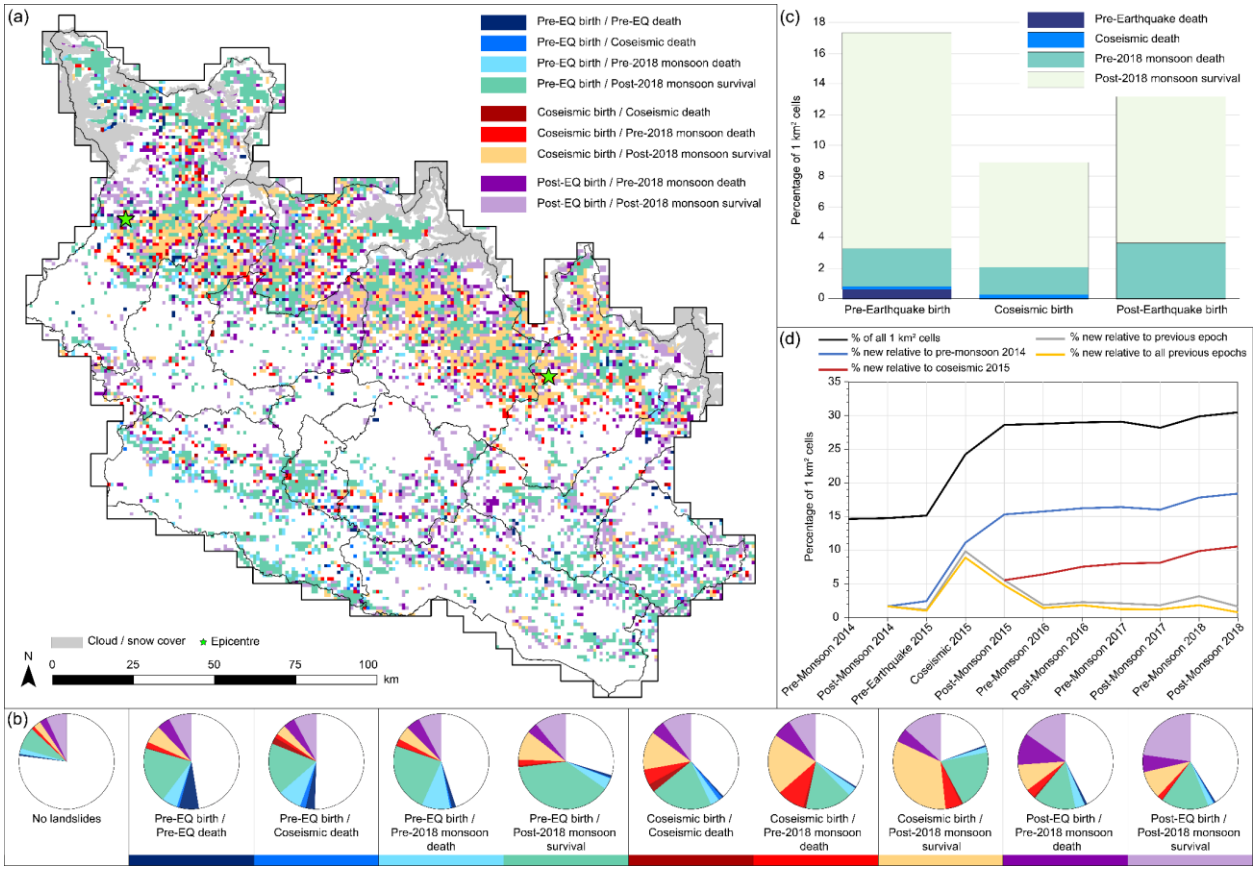

Figure 6. Spatial and temporal distributions of landslide birth and death across all 11 mapping epochs. (a) Map showing landslide birth and death categories for each 1 km^2 grid cell. The 'birth' epoch indicates the period in which the cell was first impacted by a landslide and the 'death' epoch indicates the date when the cell was last impacted by a landslide. Cool colours denote areas where landslides were born before the 2015 earthquake, warm colours denote areas where landslides were born during the earthquake, and purple shades denote areas where landslides were born after the earthquake. (b) Pie charts for cells in each birth/death category, summarising the proportion of eight neighbouring grid cells belonging to each of the other eight birth/death categories. The colour represented by each category is shown at the bottom of the panel, and corresponds to those in panel (a). A larger proportion of neighbouring cells from the same category as the central cell indicates a higher degree of spatial clustering – visible, for example for the pre-EQ birth/post-2018 monsoon survival and post-EQ birth/post-2018 monsoon survival categories. (c) Percentage of all cells belonging to each of the three birth categories, subdivided by corresponding percentage of cells from each death category. (d) Change in the proportion of cells impacted for each of the 11 mapping epochs, shown as a percentage of the total number of cells (n = 25012) and percentages relative to (i) pre-monsoon 2014 (blue line), (ii) the previous epoch (grey line), (iii) all previous epochs (orange line), and (iv) the coseismic inventory (red line).

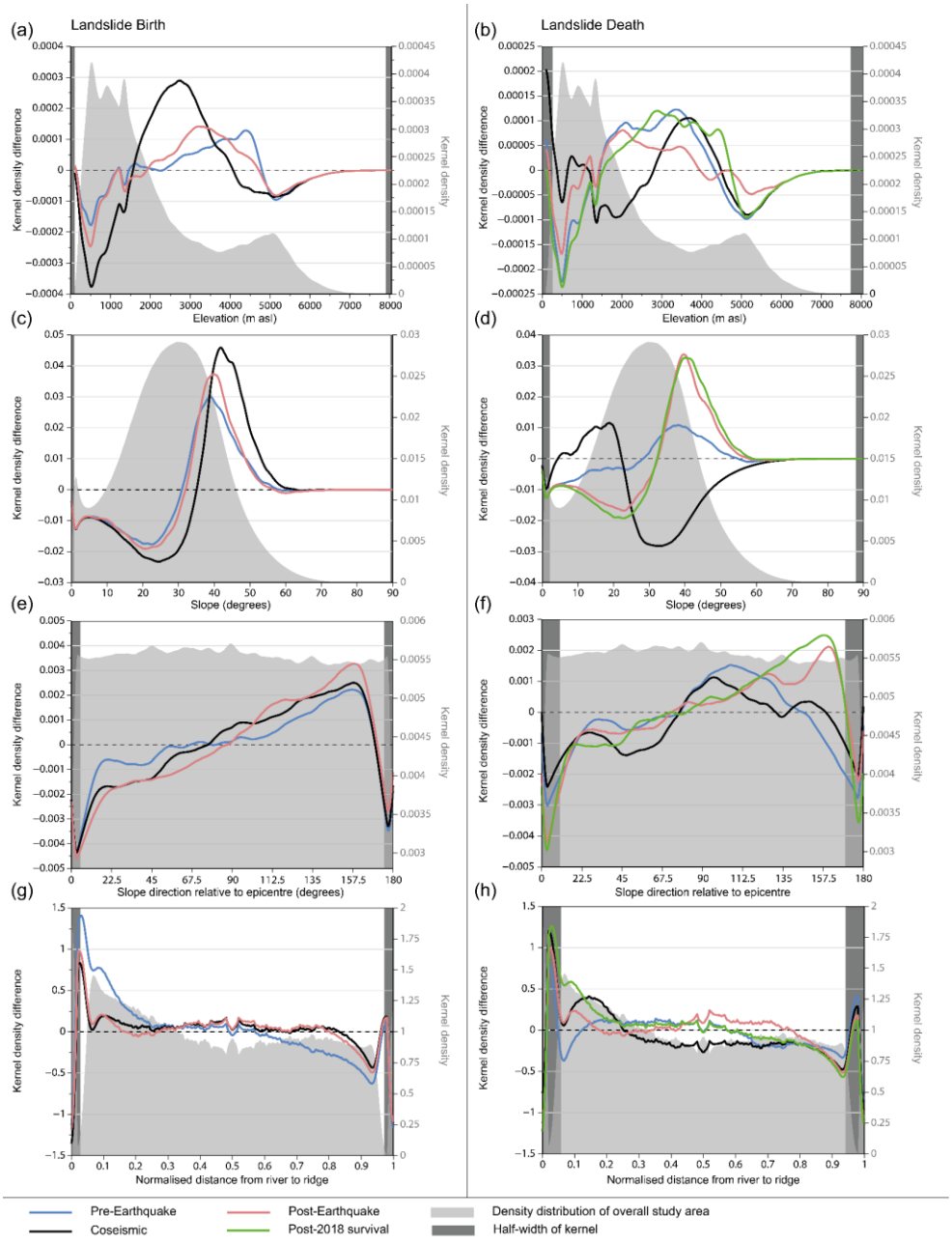

Figure 7. Topographic controls on landslide birth and death, displayed as difference in kernel density values relative to the density distribution from the overall study area. Results are shown for elevation (a,b), slope angle (c,d), slope direction relative to the Gorkha earthquake epicentre (e,f), and normalised distance from river to ridge (g,h), with the left column showing landslide birth categories and the right column showing landslide death. Difference data are based on the individual landslide polygons, with the density distribution for the overall study area shaded in light grey. Blue, black, and red lines show results for landslides in cells that were activated or recovered before, during, or after the earthquake, respectively. Green lines in the right column show results for landslides which persisted through the end of the study period, irrespective of birth epoch. The half-width of the kernel has been delimited in dark grey for each graph. Density values within these areas are likely to be less accurate due to edge effects during the density estimation. Further information on how to interpret this figure is provided in Section 6 of the Supplementary Material.

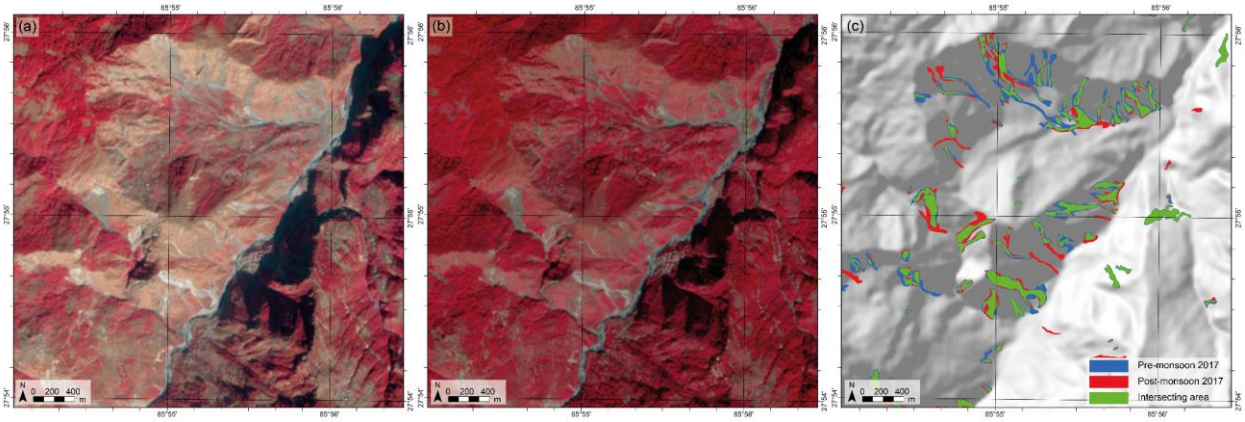

Figure 8. Detailed view of the upper Bhote Kosi, Sindhupalchok district, showing the influence of seasonal vegetation extent and character on the definition of landslide scars. (a) Pre-monsoon 2017 and (b) post-monsoon 2017 Sentinel-2 imagery of the area. (c) Mapped polygons derived from the images in (a) and (b), indicating that pre-monsoon landslides are routinely mapped as slightly larger than their post-monsoon equivalents. Sentinel-2 imagery is from the European Space Agency – ESA / Copernicus Sentinel data (2018). Digital elevation data are based on the 30-m ALOS DEM (Credit: AW3D30 – JAXA).

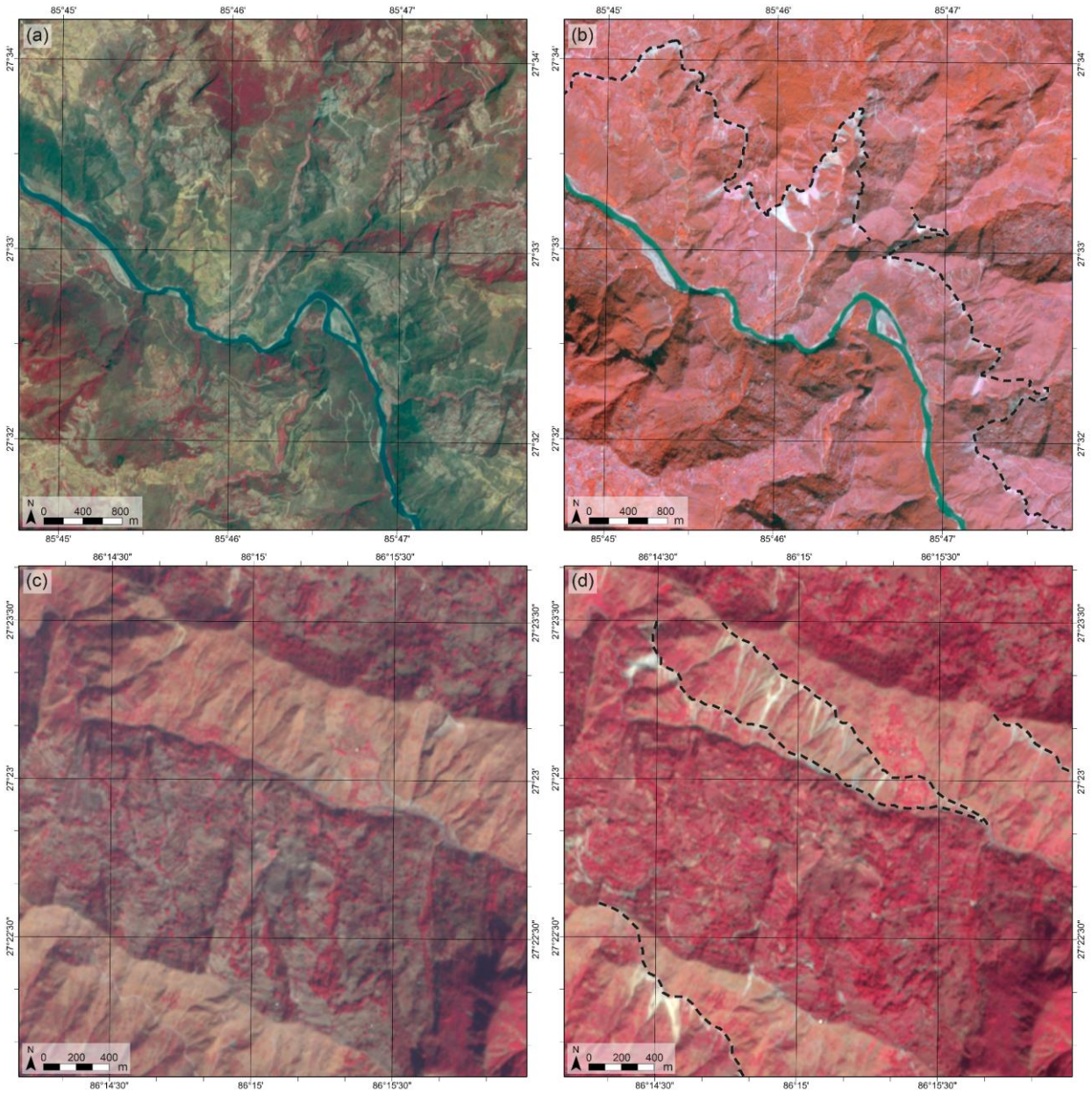

Figure 9. Examples of new landslides caused by road construction. (a) Pre-monsoon 2018 and (b) post-monsoon 2018 Sentinel-2 imagery of road construction along the Sun Koshi river, north-eastern Kabhrepalanchok district. (c) Pre-Monsoon 2017 and (d) post-monsoon 2018 Sentinel-2 imagery of road construction near Jholi, western Okhaldhunga district. Dashed lines in (b) and (d) show the routes of newly cut roads, while light areas show disturbance triggered by construction. The corresponding increased landslide area density results for these locations can be clearly seen in Figure 5. Sentinel-2 imagery is from the European Space Agency – ESA / Copernicus Sentinel data (2018).

Supporting Information for

Evolution of coseismic and post-seismic landsliding after the 2015 M_w 7.8 Gorkha earthquake, Nepal

Mark E. Kincey[1], Nick J. Rosser[1], Tom R. Robinson[2], Alexander L. Densmore[1], Ram Shrestha[3], Dammar Singh Pujara[3], Katie J. Oven[4], Jack G. Williams[1,5] and Zuzanna M. Swirad[1,6]

[1] Institute of Hazard, Risk, and Resilience and Department of Geography, Durham University, Durham, UK

[2] School of Geography, Science, and Politics, Newcastle University, Newcastle-Upon-Tyne, UK

[3] National Society for Earthquake Technology-Nepal, Kathmandu, Nepal

[4] Department of Geography and Environmental Sciences, Northumbria University, Newcastle-Upon-Tyne, UK

[5] Willis Towers Watson, Friars Street, Ipswich, Suffolk, UK

[6] Scripps Institution of Oceanography, University of California San Diego, La Jolla, CA, USA

Contents of this file

Supplementary Material 1: Landslide inventory summary statistics

For each of the eleven individual epochs, all visible landslides were manually mapped as vector polygons based on their appearance on medium resolution optical satellite imagery (Table S1, mapped count). Where the ground was obscured by cloud cover, shadowing or poor image contrast, a forward propagation approach was used to infer the presence of missing landslides in epoch *n* based on their appearance in epochs *n*-1 and *n*+1 or *n*+2 (Table S1, inferred count). This resulted in a spatially consistent set of complete landslide inventories spanning the entire area of interest (Table S1, total count). Full details of the methodology involved in this workflow are provided in Section 3.1 of the paper.

Table S1. Landslide count and area statistics for the eleven mapping epochs.

Epoch name	Mapped Count	Inferred Count	Inferred %	Total Count	Area Sum (km^2)
Pre-Monsoon 2014	6468	0	0.0	6468	66.25
Post-Monsoon 2014	5698	655	10.3	6353	62.84
Pre-Earthquake 2015	4283	2094	32.8	6377	64.79
Coseismic 2015	13191	493	3.6	13684	154.68
Post-Monsoon 2015	17613	757	4.1	18370	179.03
Pre-Monsoon 2016	18244	734	3.9	18978	164.76
Post-Monsoon 2016	17114	1281	7.0	18395	142.19
Pre-Monsoon 2017	16669	986	5.6	17655	158.59
Post-Monsoon 2017	14826	2044	12.1	16870	137.00
Pre-Monsoon 2018	17297	1293	7.0	18590	155.81
Post-Monsoon 2018	18592	0	0.0	18592	156.82

Supplementary Material 2: Landslide mapping training

To minimise errors during the construction of the landslide inventories, the two primary mappers were initially trained through repeat delineation of landslides within a 2,500 km^2 area spanning a range of physiographic settings and landslide densities (Fig. S1). Each training zone was manually checked by independent analysts following initial mapping and detailed feedback was provided to the primary mappers. Upon completion of each epoch, every 5 x 5 km grid cell was then manually checked and edited by a team of nine analysts who were independent of the primary mapping work.

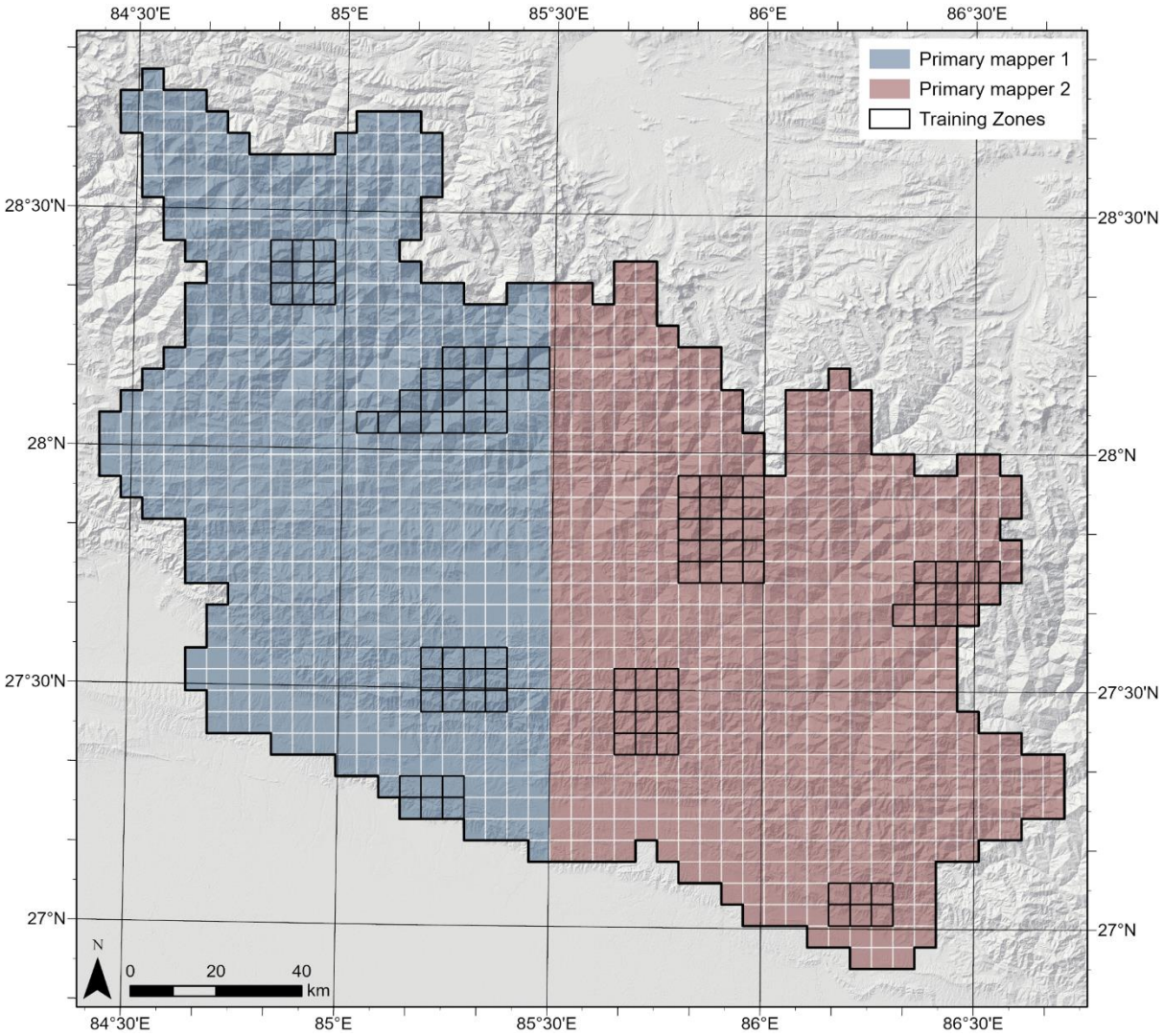

Figure S1. Map showing the overall 5 x 5 km fishnet grid used for the landslide mapping work, including the division by primary mapper and the locations of the zones comprising the 2,500 km^2 area used to iteratively train the mappers. Digital elevation data are based on the 30-m ALOS DEM (Credit: AW3D30 – JAXA).

Supplementary Material 3: Comparison with higher resolution Gorkha earthquake landslide inventory (Roback et al., 2018)

The coseismic inventory generated by Roback et al. (2018) represents the most detailed assessment of landsliding triggered by the Gorkha earthquake, both in terms of the areal extent covered by their analysis (28,300 km^2) and the image resolution used for the mapping (0.2-0.5 m). To directly compare our coseismic inventory (epoch 4) with the inventory generated by Roback et al. (2018), we first restricted the two inventories to just the spatial extent covered by both areas of interest. This included removing all areas of obscured ground (e.g. cloud cover) from both mapping extents, leaving a final intersecting area of 18,087 km^2 (Fig. S2). Analysis of the remaining landslides from within the intersecting area included a visual comparison of the spatial coincidence and morphological characteristics of the two inventories within ArcGIS 10.5 (e.g. Fig. S3), and export of the size characteristics of the polygons for subsequent area-frequency comparison.

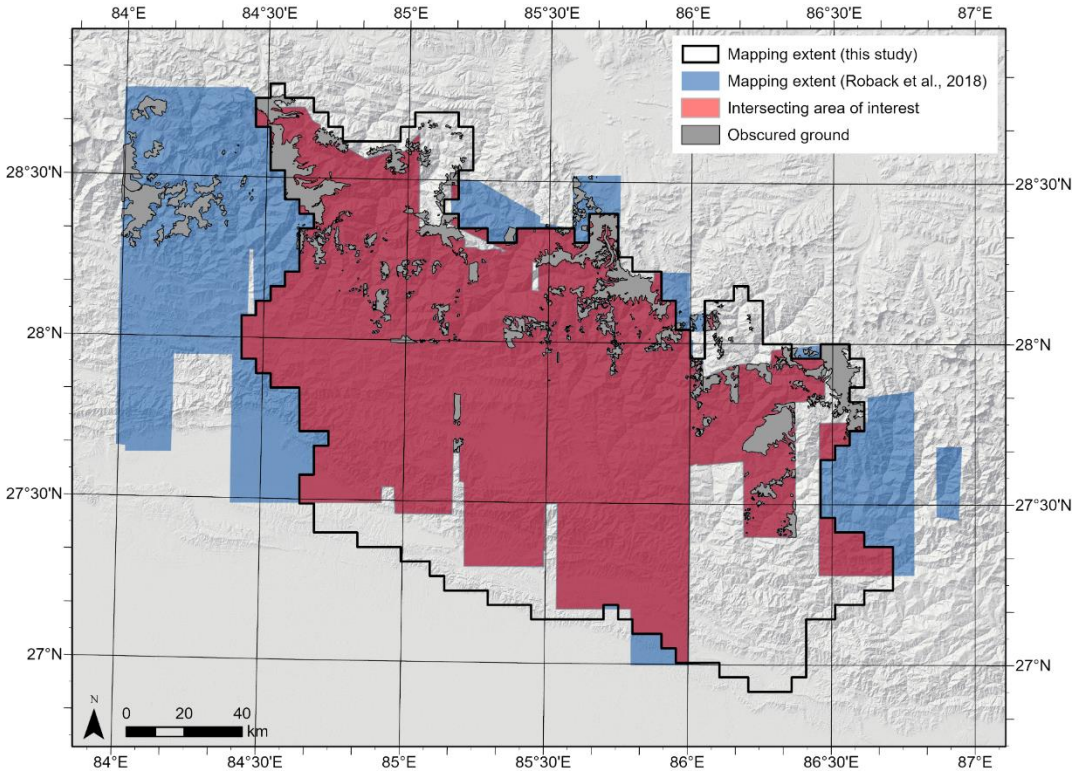

Figure S2. Map showing the mapping extent for our inventory (black outline), the Roback et al. (2018) inventory (blue) and the intersecting area used for the comparative analyses (red) Digital elevation data are based on the 30-m ALOS DEM (Credit: AW3D30 – JAXA).

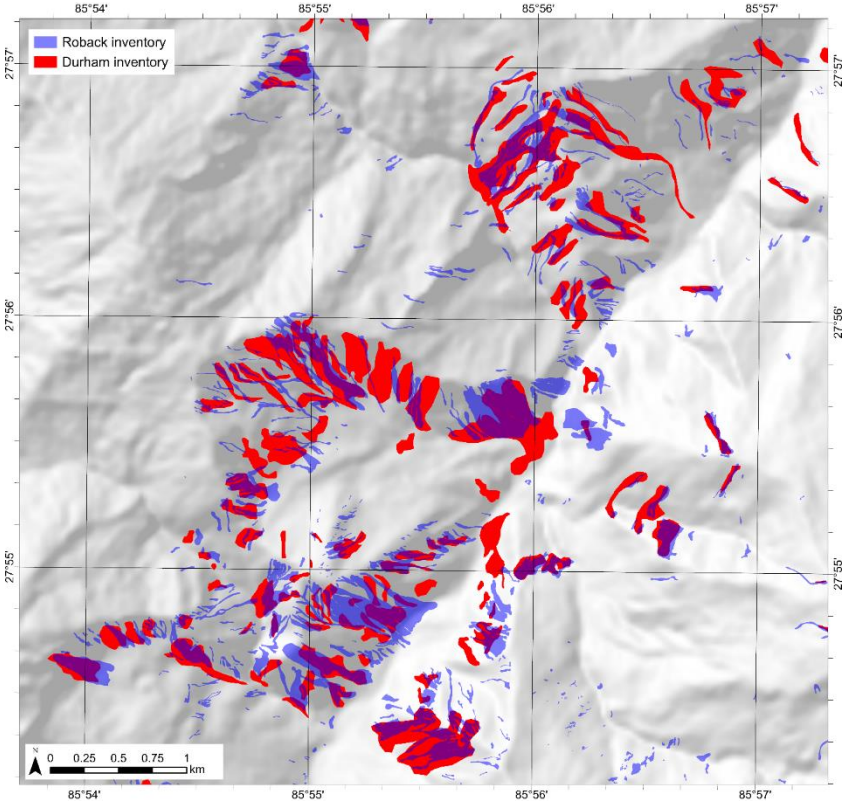

Figure S3. Map showing an example subset area within the upper Bhote Kosi valley in Sindhupalchok district, with a comparison overlay of our coseismic inventory in red and that generated by Roback et al. (2018) in blue. Digital elevation data are based on the 30-m ALOS DEM (Credit: AW3D30 – JAXA).

The area-frequency characteristics of the two inventories were examined through comparison of power-law scaling relationships obtained using the 'powerlaw' Python package (Alstott et al., 2014), which is based on the statistical methods developed in Clauset et al. (2009). Probability density distributions of landslide area were calculated for each inventory, along with the minimum landslide area threshold beyond which the power-law relationship can be reliably defined (x_min) and the power-law scaling exponent (α). The probability density distributions are shown in Fig. S4, with the corresponding power-law scaling parameters shown in Table S2.

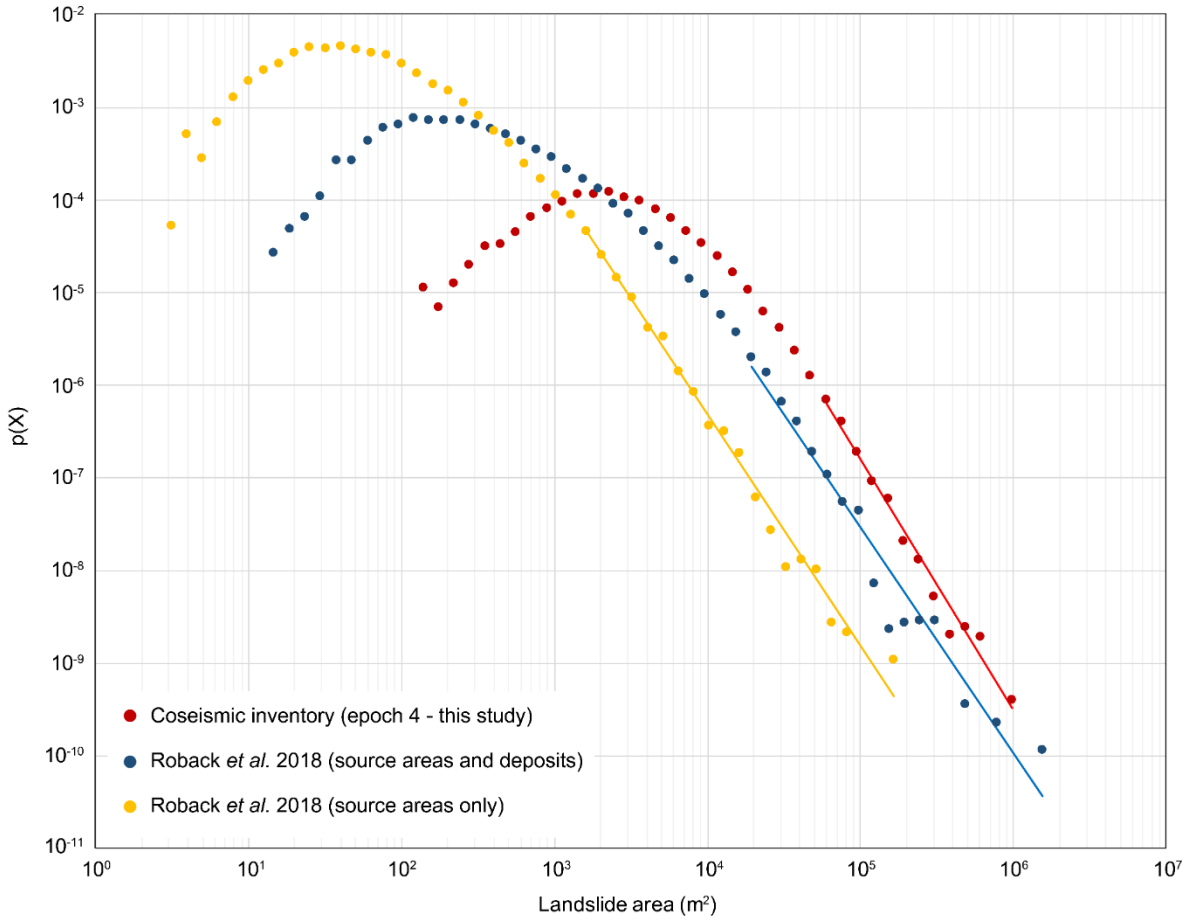

Figure S4. Probability density distributions of landslide area for our coseismic landslide inventory (red) and those produced by Roback et al. (2018), including their combined inventory comprising both source areas and deposits (blue) and source areas alone (yellow). Best-fit power-law trends for the tails of the distributions are displayed, with corresponding scaling parameters shown in Table S2.

Table S2. Power-law scaling parameters (minimum size threshold and power-law exponent) for our coseismic landslide inventory and that produced by Roback et al. (2018)

Inventory	Image resolution for mapping (m)	Best-fit x_min	Best-fit exponent α
Coseismic inventory (this study)	15	48,413	2.93
Roback *et al.* 2018 (source areas and deposits)	0.2-0.5	18,446	2.74
Roback *et al.* 2018 (source areas only)	0.2-0.5	1,338	2.49

Supplementary Material 4: Influence of satellite image resolution on landslide inventory characteristics

The influence of satellite image resolution on landslide inventory characteristics was assessed through repeat mapping of a 121 km^2 subset area within the upper Bhote Kosi valley, Sindhupalchok (Fig. S5). All visible landslides were mapped from four different image tiles of varying spatial resolution (Table S3), with the mapping being done by a single analyst but with no reference to any of the other images or derived inventories in each case. The highest resolution image was a 2 m resolution Pleiades tile captured on 30 Sept 2015, which is coincident with epoch 5 of the multi-temporal inventory. To simulate the influence of changing spatial resolution, the Pleiades tile was then resampled via cubic convolution to 10 m resolution, which is equivalent to the R-G-B-NIR Sentinel-2 bands, and to 15 m resolution, which is equivalent to the spatial resolution of a pan-sharpened R-G-B-NIR Landsat 8 image. For comparison, mapping was also undertaken for an independent 15 m pan-sharpened Landsat 8 image tile captured on 7 Oct 2015. In each case the images were displayed as false colour composites based on the green, red and near-infrared bands and mapping was conducted by delineating landslides as vector polygons within ArcGIS 10.5.
Area-frequency characteristics were examined by fitting power-law scaling relationships to each of the four datasets using the same 'powerlaw' Python package outlined above (Supplementary Material 3). The probability density distributions for each of the resolution inventories are displayed in Fig. S6, with the corresponding power-law scaling parameters shown in Table S3. Summary statistics by image resolution are then displayed in Fig. S7, including the number of landslides per inventory, the total area of landsliding as a percentage of the inventory derived from the 2 m image, and the mean and standard deviation of landslide size for each inventory.

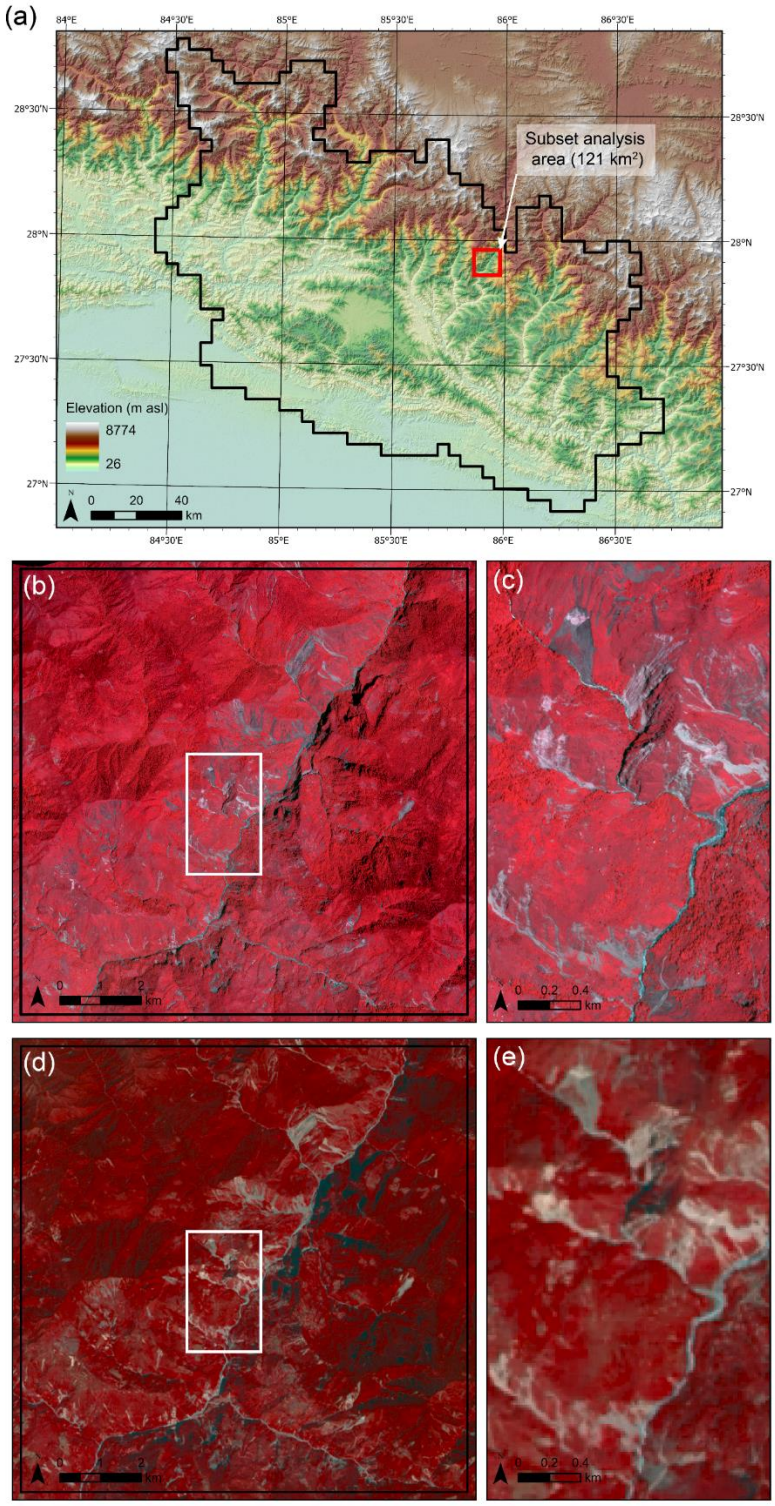

Figure S5. Map showing the 121 km^2 subset area used to assess the influence of image spatial resolution on inventory characteristics. (a) Location of the analysis area (red box) within the overall mapping extent, overlain on shaded relief elevation map derived from 30 m ALOS DEM. (b) Pleiades image tile (2 m resolution) covering the extent of the subset area. The white box shows the extent of the detailed Pleiades image shown in (c). (d) Pan-sharpened Landsat 8 image tile (15 m resolution) for the same area, with the white box showing the same detailed extent shown in (e). Pleiades imagery includes material © CNES (2015), Distribution Astrium Services / Spot Image S.A., France, all rights reserved. Landsat 8 image courtesy of the U.S. Geological Survey. Digital elevation data are based on the 30-m ALOS DEM (Credit: AW3D30 – JAXA).

Table S3. Image characteristics and acquisition dates used in the assessment of the influence of spatial resolution on derived inventory characteristics. Power-law scaling parameters (minimum size threshold and power-law exponent) for each inventory are provided and refer to the power-law trends shown in Fig. S6.

Image resolution (m)	Satellite / sensor	Acquisition date	Description	Best-fit x_min	Best-fit exponent α
2	Pleiades	30/09/2015	4-band high spatial resolution multispectral image (R-G-B-NIR)	8,034	2.26
10	Pleiades	30/09/2015	2 m Pleiades data resampled to 10 m resolution using cubic convolution resampling. Equivalent spatial resolution to R-G-B-NIR Sentinel-2 imagery.	26,369	2.82
15	Pleiades	30/09/2015	2 m Pleiades data resampled to 15 m resolution using cubic convolution resampling. Equivalent spatial resolution to pan-sharpened Landsat imagery.	10,865	2.23
15 / 30	Landsat 8	07/10/2015	4-band multispectral Landsat 8 dataset (R-G-B-NIR). 30 m spatial resolution for standard bands, pan-sharpened to 15 m using the panchromatic band (B8).	15,526	2.41

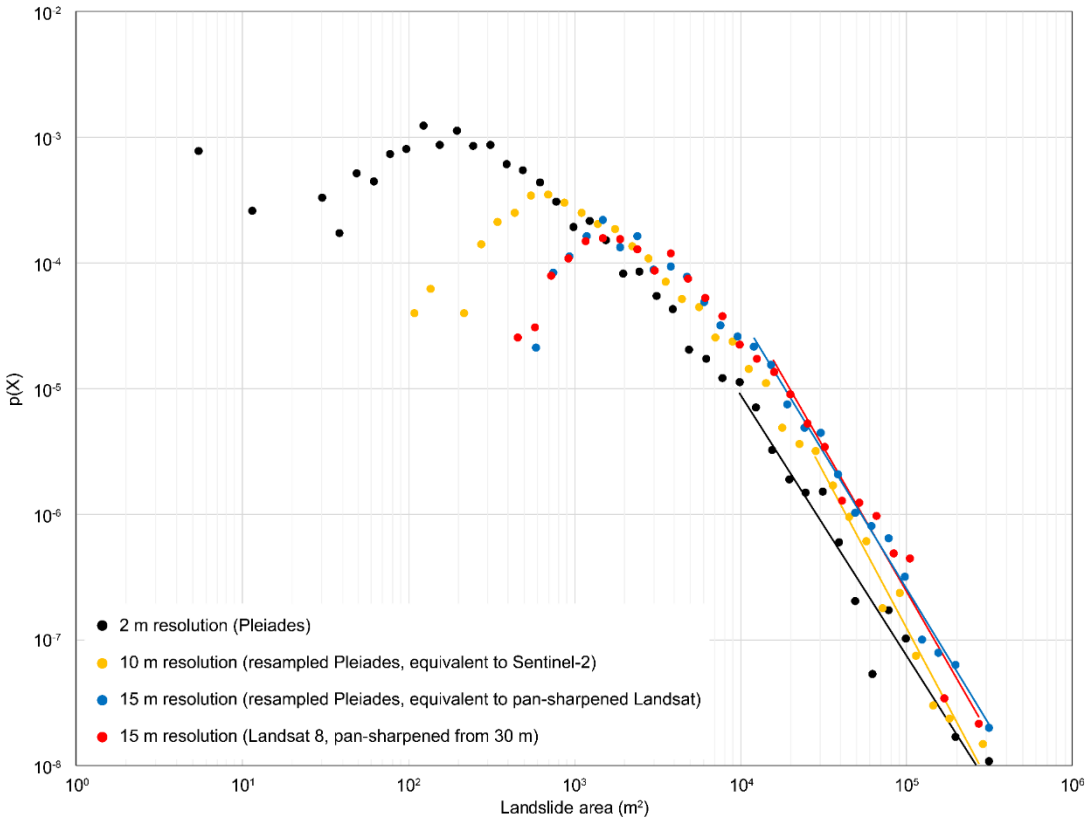

Figure S6. Probability density distributions of landslide area for each of the four inventories used in the assessment of image spatial resolution. Best-fit power law functions for the tails of the distributions are displayed, with corresponding scaling parameters shown in Table S3.

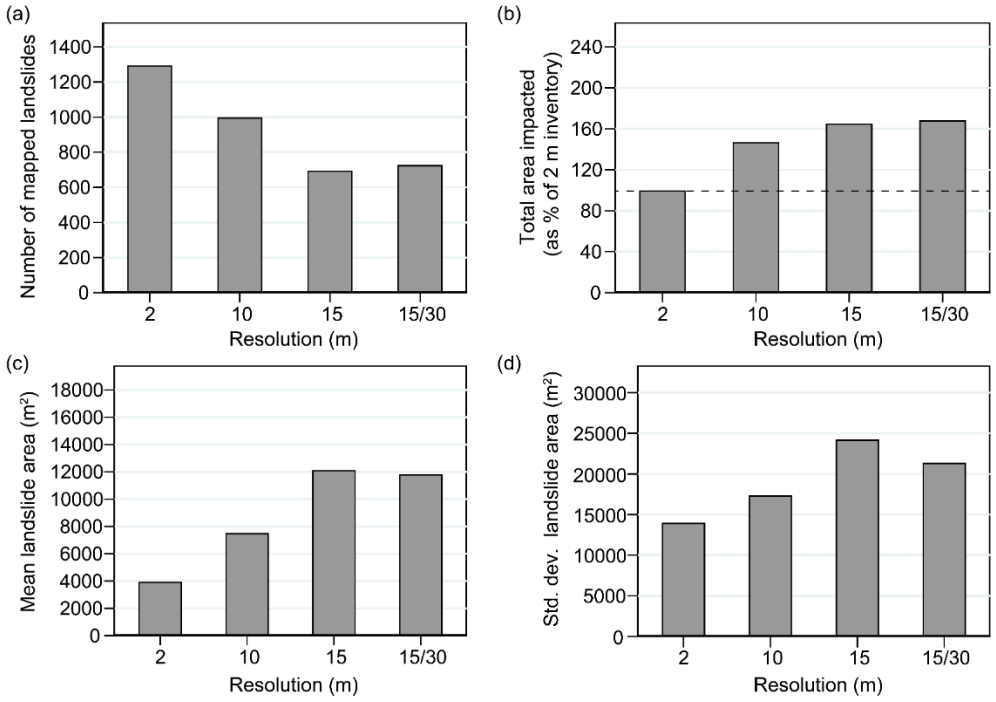

Figure S7. Summary statistics derived from the four inventories used in the assessment of image spatial resolution. (a) The total number of landslides mapped in each inventory. (b) The total area impacted as a percentage of the 2 m Pleiades inventory. (c) Mean landslide area and (d) standard deviation of landslide area for each of the four inventories.

Supplementary Material 5: Rainfall time series

Rainfall data for the period 2014 to 2018 were obtained from NASA's Global Precipitation Measurement (GPM) Integrated Multi-satellitE Retrievals for GPM (IMERG) data, accessed via https://pmm.nasa.gov/data-access/downloads/gpm. Data were downloaded as gridded monthly NetCDF files at a spatial resolution of 0.1°, equivalent to a pixel size of approximately 11 km^2. Individual monthly files were converted to geotiffs and analysed within ArcGIS 10.5 to extract relevant precipitation metrics, including per-pixel annual totals and means, and overall summary statistics including annual totals, annual monsoonal totals and mean monthly totals (Fig. S8).

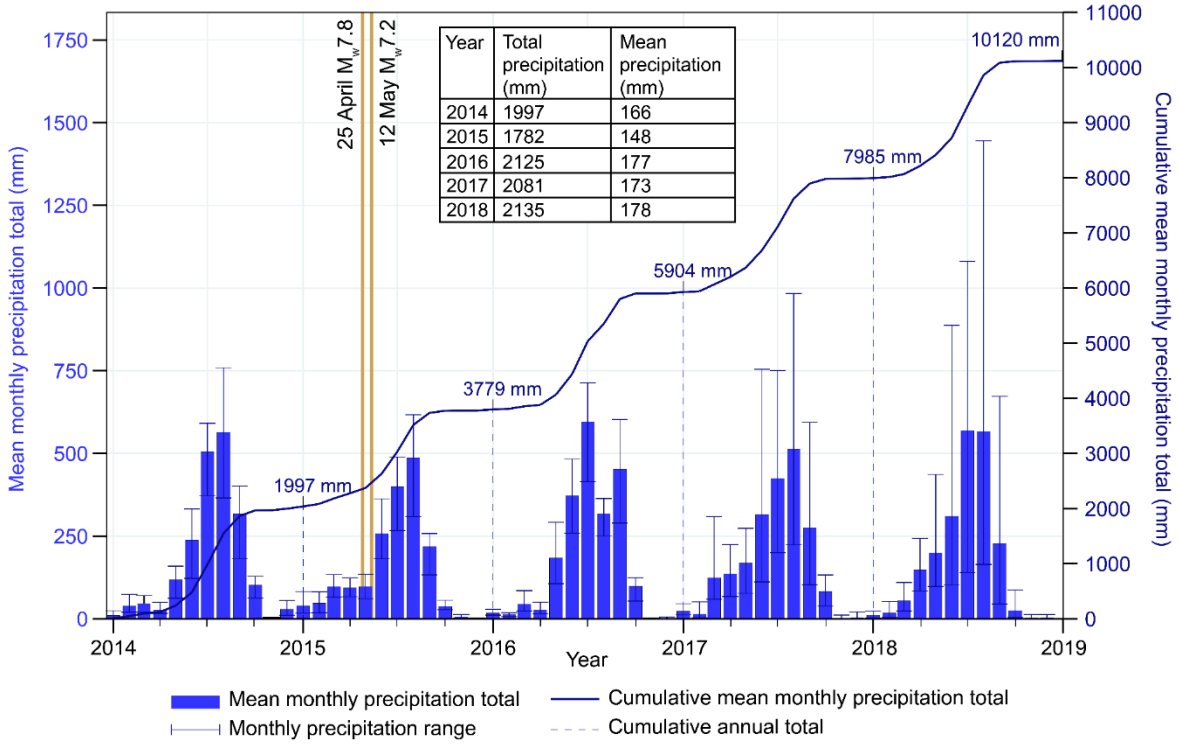

Figure S8. Rainfall time series for the period 2014-2018. Mean monthly rainfall totals and total ranges are displayed as vertical bars and spikes respectively, with cumulative totals provided for reference. Inset table provides total annual precipitation and mean annual precipitation. Vertical orange lines indicate the dates of the M_w 7.8 Gorkha earthquake (25 April 2015) and the major M_w 7.2 aftershock (12 May 2015).

Supplementary Material 6: Kernel density differencing

The assessment of potential topographic controls on landsliding was based on the differencing of multiple kernel density estimations. For each topographic metric, kernel density estimates were calculated at 500 equal intervals along the full range of potential values for the entire study area. As an example, given a hypothetical range of elevation values of 0 to 8000 m within the overall study area, kernel density values would be estimated at points every 16 metres along this elevation range. The kernel density estimation was then re-run for each birth and death sub-category of the overall inventory polygon data but with the density estimations again calculated at the same 500 elevation values. Since kernel density estimation is based on a moving window analysis the size of the window, typically defined by the half-width *h*, is important as it determines

the degree of smoothing, with larger values resulting in smoother density curves but potentially at the expense of local bias, where localised detail can be under- or over-estimated (Cox 2007). The half-width of the moving kernel was therefore kept constant for all density estimations for each topographic variable.

This approach provides kernel density estimates for specific topographic variables that can then be compared between multiple input datasets. Differences between the overall study area and the landside birth and death categories were calculated by subtracting the study area density values from each equivalent landslide subset density value. Negative values indicate that landslides occur less frequently than would be expected from a random distribution. Positive values mean that landslides in that class occur more frequently than would be typically expected. Since each birth and death category is differenced separately, the difference curves are independent of each other and can therefore be directly compared. As an example, more than 46% of the mapping area had an elevation <1500 m but landslides are relatively uncommon in these areas, meaning that the density distribution for all landslide birth categories is negative within the range 0 – 1500 m (Fig. S9).

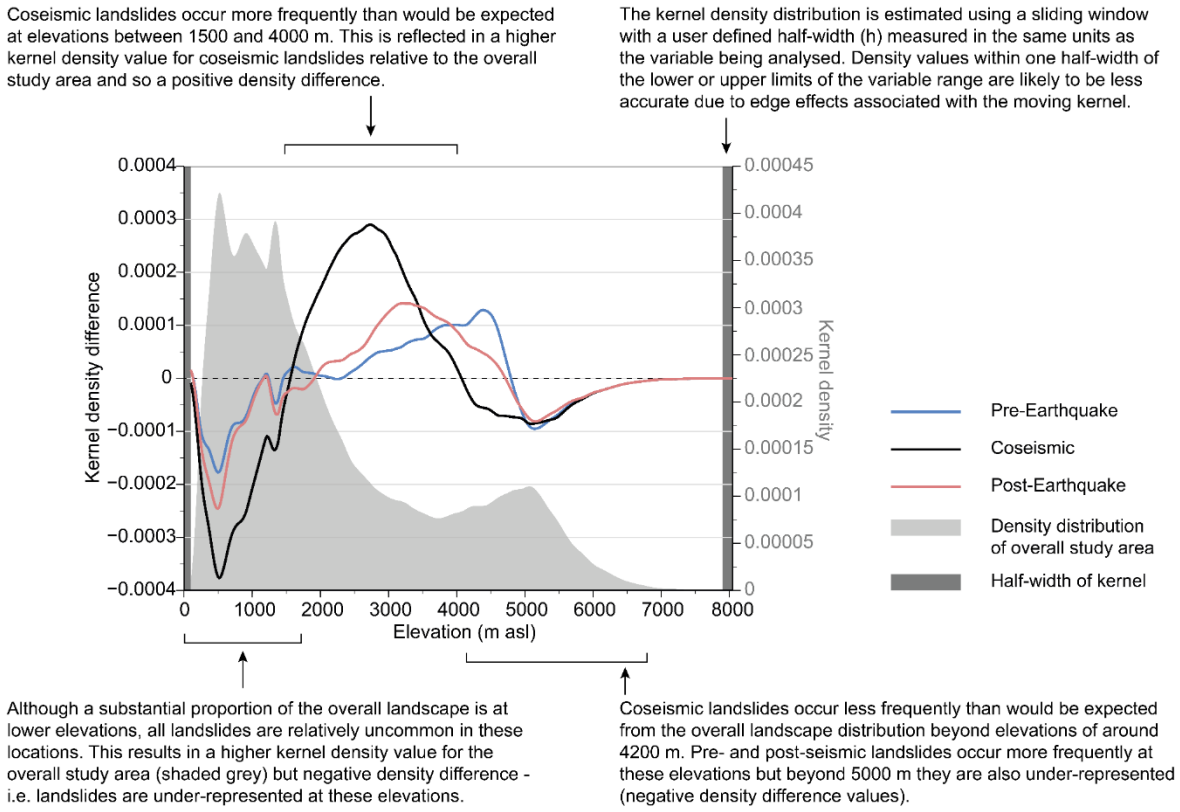

Figure S9. Example kernel density differencing output showing how landslide birth categories differ by elevation. Explanatory notes are included to provide additional information on how to interpret the difference graphs shown in Figure 7.

Supplementary Material 7: Pixel-based landslide birth and death analysis

The calculated rate of landscape recovery following a large earthquake is fundamentally dependent on how recovery is defined and measured. In our study we mapped all landslides visible on each epoch of imagery, treating each inventory independently and without reference to whether a landslide was already present at that location in a previous epoch (Section 3.1). This approach differs from other studies which have only mapped the occurrence of new landslides, or attempted to qualitatively assess the degree of reactivation of coseismic landslides (Section 5.1).

To demonstrate the importance of the methodology employed for the mapping and analysis of multi-temporal landside inventories, here we briefly present the results of an alternative approach to analysing our inventory time series. This approach involved converting landslide polygons from all epochs to 10 m resolution rasters, which was equivalent to the mapping resolution when using Sentinel-2 imagery. Each 10 x 10 m cell was then assigned a value for landslide birth (the first epoch in which that cell was intersected by a landslide), landslide death (the last epoch in which that cell was intersected by a landslide), and landslide persistence (the number of epochs in which that cell was intersected by landslides) (Fig. S10). Based on these datasets, other summary statistics were also generated, such as the cell-wise epoch range (the difference between the minimum and maximum epochs) and the standard deviation, which was derived from a stack of reclassified rasters where a value of '1' represents landslides and '0' represents no landslide.

Summary statistics derived from these rasters provided the number of new landslide cells that were born within each epoch and the number which died by the subsequent epoch, representing the per-epoch cell birth and death counts respectively (Fig. S11a-b). In this case the rate of new landslide activity is defined as including all 10 x 10 m cells relating to either entirely new failures and/or the expansion of existing landslides. This approach to assessing recovery rate is closely comparable to multi-temporal studies which only map the occurrence of either new landslides (e.g., Marc et al., 2015, 2019) or clearly detectable reactivation of pre-existing landslides (e.g., Li et al., 2018; Fan et al., 2018). Persistence was assessed through quantifying the recurrence of landsliding for each cell through consecutive epochs, for example in epoch *n* and epoch *n*-1 (Fig. S11c). The difference between the landslide cell birth and death counts for each epoch then provided an alternative measure of how quickly the landscape was recovering, at least in terms of the net change in the number of cells being newly impacted versus those which were no longer intersected by landslides (Fig. S11d). For a broader discussion of the relative merits of the different approaches to assessing landscape recovery following a large earthquake see Section 5.1.

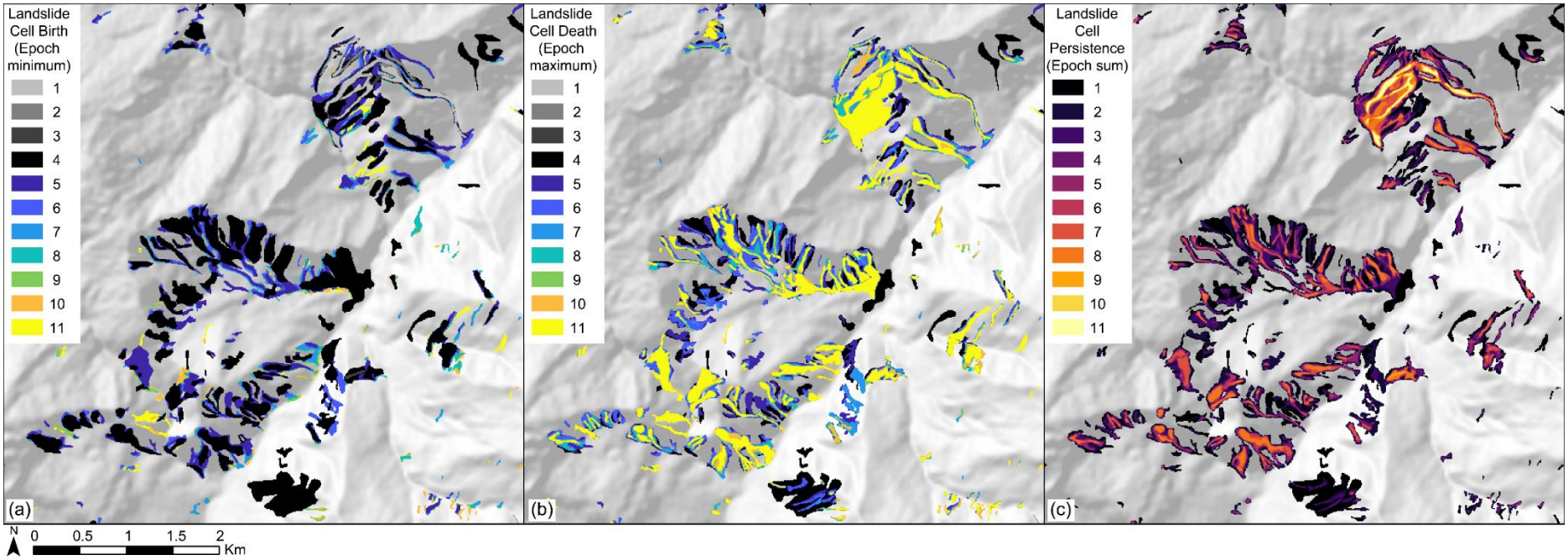

Figure S10. Example output from the cell-based analysis of landslide change through time. (a) Landslide cell birth, defined as cell earliest epoch in which a cell was intersected by a landslide. (b) Landslide cell death, defined as the latest epoch in which a pixel was intersected by a landslide. (c) Landslide persistence, calculated as the cell-wise count of the number of epochs in which that location was intersected by a landslide. Digital elevation data are based on the 30-m ALOS DEM (Credit: AW3D30 – JAXA).

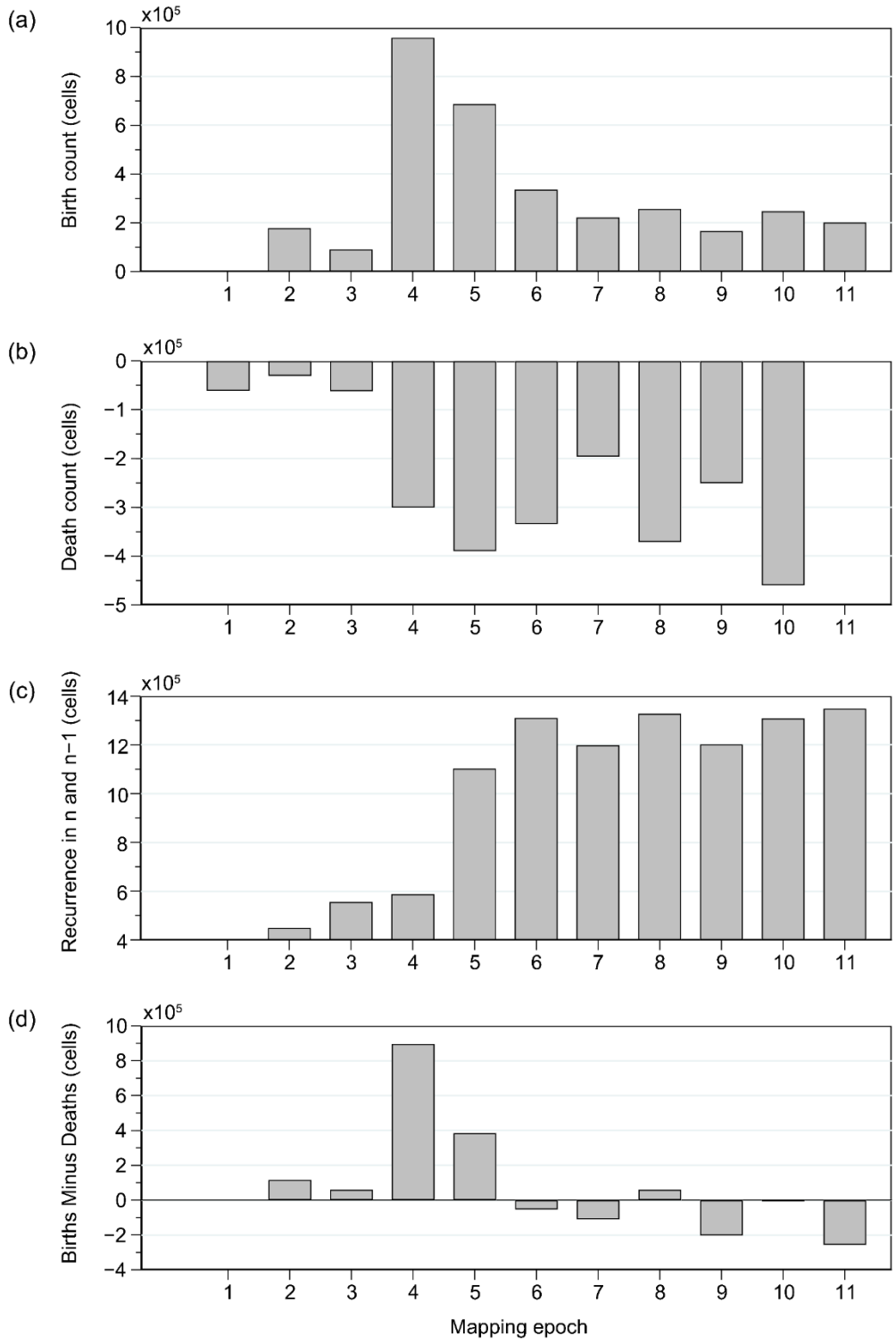

Figure S11. Summary of cell-based landslide birth and death analysis. (a) The number of cells that were newly impacted by landslides in each epoch (landslide birth). (b) The number of cells that were last impacted by landslides for each given epoch (landslide death). (c) The number of landslide cells that were also impacted by landslides in the previous epoch. (d) The per-epoch difference in the overall cell-based landslide birth and death counts